

The effect of geometry on resistance in elliptical coaxial pipe flows

J.G. Williams¹, B.W. Turney², D.E. Moulton¹, and S.L. Waters^{1*}

¹Mathematical Institute, University of Oxford, Oxford OX2 6GG, UK

²Nuffield Department of Surgical Sciences, University of Oxford, OX3 9DU

(Received xx; revised xx; accepted xx)

This paper considers the significant role of cross-sectional geometry on resistance in coaxial pipe flows. We consider an axially flowing viscous fluid in between two long and thin coaxial cylinders, one inside the other. The outer cylinder is stationary, while the inner cylinder (or rod) is free to move. The inner rod thus poses a resistance to the axial flow, while the viscous fluid poses a resistance to any motion of the inner rod. The objective of this paper is to characterise the nature of these resistances and how they depend on the cross-sectional geometry. In particular, we consider three particular geometries: I) a circle inside an ellipse, II) an ellipse inside a circle, and III) an ellipse inside an ellipse. We show that the equations for flow in the axial direction – driven by a prescribed flux – and for flow within the cross-section of the domain – driven by the motion of the rod – decouple in the asymptotic limit of small cylinder aspect ratio. We can thus analyse axial and cross-sectional resistance separately, with the governing fluid equations reducing to axial Poiseuille flow and transverse Stokes flow, respectively. In the case of axial resistance, we identify geometries that minimise resistance (or equivalently maximise flux for a given pressure drop). Cross-sectional resistance can be characterised via coefficients in a Stokes resistance matrix, and we highlight several counterintuitive phenomena and nonlinear effects of the geometry. We also uncover a correlation between the rod position which minimises the axial resistance and the rod position that results in the largest resistance to rotation and transverse rod motion, and further explore this idea in terms of computed trajectories of the inner rod.

1. Introduction

Fluid flow in annular geometries is prevalent, found in a range of apparatuses from oil wells to surgical tools. Annular flows between a co-axial rod and outer cylinder motivate fundamental design questions, such as:

- 1) How to position the inner cylindrical rod to maximise axial flow?
- 2) How will the inner rod move and rotate if free to do so?
- 3) How do the answers to 1 and 2 depend on the cylinders' cross-sectional shapes?

A specific medical application of our work is found in a minimally invasive surgical procedure for the removal of kidney stones, uretero-renoscopy. This involves the insertion of long fibres, *working tools*, used to destroy or capture stones, through a long cylindrical *working channel* through which there is an axially flowing saline solution. A minuscule camera in the scope tip allows the surgeon to see inside the patient's kidney and the axially flowing fluid is required to clear the field-of-view and to open up the ureter, see Figure 1. The working channel lies within the cylindrical shaft of a *ureteroscope*, and another outer cylinder, an *access sheath*, surrounds the scope itself, allowing fluid

* Email address for correspondence: waters@maths.ox.ac.uk

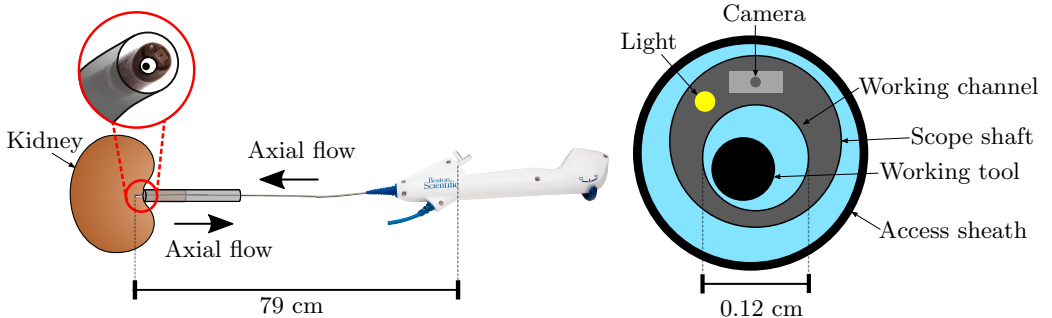


Figure 1: A photograph of an isolated Boston Scientific ureteroscope (left) with the tip of the scope circled and a zoomed-in schematic provided of the scope tip (right). The scope lies within an access sheath, and a working tool sits inside the working channel. A camera and a light are embedded in the scope wall. Dimensions of the scope shaft and working channel are labelled.

to flow back out of the kidney. Minimising the flow resistance posed by the working tools can increase flow through the working channel and subsequent surgical accuracy by improving visibility within the kidney (Williams *et al.* 2019). Minimising the flow resistance through the access sheath leads to lower kidney pressures during uretero-renoscopy (Oratis *et al.* 2018) which is desirable as high pressures have been linked to post-operative complications, such as sepsis (Wilson & Preminger 1990). This application in particular motivates us to address questions of flow optimality in the sense of achieving the maximum flow rate for a prescribed axial pressure drop and fixed cross-sectional area available for fluid flow. The possible design of elliptical access sheaths, working channels, and working tools has been motivated by the ureteral opening resembling an ellipse (Bergman 1981) and channels with elliptical cross-sections being relatively easy to manufacture. Thus, we restrict attention to cylinders with elliptical cross-sections. When designing an optimal device the ideal scenario would be to place the inner cylindrical rod in the position that minimises axial flow resistance. A key consideration is whether the surrounding fluid would then resist changes to the inner rod position, or whether the device must be designed to constrain the inner rod to the position that minimises axial flow resistance.

Our modelling framework comprises a solid cylindrical rod of mass m and effective radius R_i , rotating about, and moving in a direction perpendicular to, its longitudinal axis, within a coaxial outer cylinder of equal length, L , and comparable radius, R_o , filled with an axially flowing viscous fluid of typical flow rate Q , density ρ , and dynamic viscosity, μ . We take the cross-sections of the rod and outer cylinder to be ellipses of varying eccentricities; this is both appropriate for our uretero-renoscopy application and allows us to investigate the effects of non-axisymmetry. Typical parameter values for ureteroscopy irrigation, which will guide our analysis here, are listed in Table 1. Defining the radius-to-length ratio of the rod as $\epsilon = R_i/L$ and the Reynolds number of the flow as $\text{Re} = QL\rho/\mu R_i^2$, the key parameters governing the behaviour of the fluid and the inner rod are ϵ^2 , $\epsilon^2 \text{Re}$, and the ratio of fluid-to-rod mass multiplied by the reduced Reynolds number, $\alpha^{-1} = (m/\rho R_i^2 L)\epsilon^2 \text{Re}$. Using typical values presented in Table 1, we find $\epsilon^2 = \mathcal{O}(10^{-5} - 10^{-6})$, $\epsilon^2 \text{Re} = \mathcal{O}(10^{-1})$, and $\alpha^{-1} = (10^0)$. These suggest that fluid inertia is negligible while rod inertia is not. In this regime, we show that the axial fluid flow through the annular region and the cross-sectional flows induced by the perpendicular movement and rotation of the rod can be decoupled into axial Poiseuille flow and

	Symbol	Value	Unit
Scope in sheath	R_o	1.9×10^{-1}	cm
	R_i	1.6×10^{-1}	cm
	L	3.6×10^1	cm
	m	6.1×10^0	g
Tool in working channel	R_o	6.0×10^{-2}	cm
	R_i	2.2×10^{-2}	cm
	L	7.9×10^1	cm
	m	1.1×10^0	g
Fluid properties	Q	1.0×10^{-1}	cm^3/s
	ρ	1.0×10^0	g/cm^3
	μ	1.0×10^{-2}	$\text{g}/\text{cm s}$

Table 1: Table of typical parameter values for ureteroscopy irrigation. For a scope in a sheath, R_o is a typical effective radius of the access sheath (11/13 F Navigator, Boston Scientific; 1 F corresponds to three times the diameter in millimeters) and R_i and m are a typical effective radius of the scope shaft and its mass, respectively (LithoVue, Boston Scientific). For a tool in a working channel, R_o is a typical effective radius of the working channel (LithoVue, Boston Scientific) and R_i and m are a typical effective radius of a working tool and its mass, respectively (ZeroTip 3.0 F, Boston Scientific). Fluid properties are those of water, and the flow rate Q follows typical bench-top experiments of flow through a working channel (Williams *et al.* 2019).

Stokes flow in the cross-section. The motion of the rod is determined by conservation of linear and angular momentum, incorporating the hydrodynamic resistance exerted by the surrounding viscous fluid. Within this setup, our objective is to investigate the nature of the resistance, both the cross-sectional resistance to the motion of the inner rod and resistance to the axial flow, in terms of the geometry of the two cylinders. In particular, we consider

- I) a circular rod inside an elliptical cylinder,
- II) an elliptical rod inside a circular cylinder, and
- III) an elliptical rod inside an elliptical cylinder.

The literature on viscous-dominated fluid flows through annular pipes is vast. A description of relevant literature is given below and summarised in Table 2. As our primary concern is the effect of cross-sectional geometry on resistance, we have grouped references by geometry in Table 2, and have further distinguished which previous works have studied axial versus cross-sectional flow and motion of the inner rod.

1.1. Axial flow resistance

An analytical solution exists for the steady, fully-developed (Poiseuille) flow of a viscous fluid through an annular region formed by concentric circles (Lamb 1916). By employing conformal maps, analytical solutions have also been obtained in a domain bounded by non-concentric circles (Heyda 1959; Sastry 1964; Shivakumar & Chuanxiang 1993; MacDonald 1982). Numerical solutions for the flow in these domains, together with the corresponding wall shear stress distributions, have also been obtained (Redberger 1962; Ebrahim *et al.* 2013; Snyder & Goldstein 1965). These solutions demonstrate that the distance between the centres of the bounding circles significantly affects the

velocity distribution, and that the total flux for fixed pressure drop increases with this metric. Analytical solutions for steady, viscous flow through annular ducts bounded by confocal ellipses, and externally by an ellipse and internally by a circle (with coincident centres) have also been determined by employing conformal maps (Sastry 1964), although the dependence of the flow rate on the geometry of the domain was not discussed. Shivakumar & Chuanxiang (1993) also considered a region bounded internally by a circle and externally by an ellipse and noted a flux enhancement compared to cross-sections bounded by two concentric circles or two confocal ellipses of the same cross-sectional area. Flow through an annular region bounded by non-concentric ellipses or by an ellipse in a circle, which form key components of our analysis, has not been previously considered (see Table 2).

1.2. Cross-sectional flow resistance

Two-dimensional Stokes flow between two circular cylinders has been well-studied (Jeffrey 1922; Jeffrey & Onishi 1981; Frazer 1926; Chwang & Wu 1975; Wannier 1950; Slezkin 1955). The dynamics of a viscous fluid confined in the gap between rotating cylinders, i.e. Taylor-Couette flow, has many mechanical applications, e.g. to the lubrication of rotary bearing systems. Stokes flow due to a line rotlet (a rotating circular cylinder of infinitesimal radius) inside an elliptic cylinder was solved analytically by Hackborn (1991). The results focussed on the resulting flow structure and it was found that the number of eddies in the cross-section produced by the line rotlet increased approximately linearly with the ratio of length to width of the outer elliptical cross-section. Hackborn (1991) postulated that the flow features generated by a line rotlet inside a fixed elliptic cylinder are expected to persist when the line rotlet is replaced by a rotating circular cylinder. Stokes flow between rotating confocal ellipses has also been considered (Saatdjian *et al.* 1994), and an analytical solution for the stream function obtained using elliptical cylindrical coordinates. It was shown that for counter-rotating ellipses, two hyperbolic points appear in the flow.

As the elliptical eccentricity of the outer cylinder cross-section tends to 1, the domain approximates one of parallel plates. The motion of a rod of circular cross-section rotating and translating in Stokes flow between parallel plates has been studied numerically (Dvinsky & Popel 1987). The authors computed the position between the centreline and the wall where the rod experienced the minimum translational drag. It was also found that the torque on a cylinder rotating between parallel plates is minimised when the cylinder is centred between the two walls. An asymptotic solution (for small gap between the cylinder and the walls compared to the cylinder radius) for a circular cylinder rotating between parallel plates was obtained by Yang *et al.* (2013). It was shown that if the cylinder is centred between the two plates, rotation will only induce an opposing torque, whereas if the cylinder is offset from the centreline, there is an additional force parallel to the walls.

Two-dimensional Stokes flow in a bounded annular domain with a translating and rotating inner rod has also been considered. Finn & Cox (2001) presented an analytical solution for the stream function for such a flow when both the inner rod and outer cylinder have circular cross-sections. The biharmonic equation for the stream function was solved with complex variable methods. The motion of the cylindrical rod was prescribed as a function of time, and the energy required to maintain the system in equilibrium was determined. It was shown that the power input depends upon the position of the rod and the prescribed motion. As the two cylinders approach each other, the power input required to maintain all motions diverges. Cox & Finn (2007) considered multiple rods with elliptical cross-sections moving inside a circular cylinder via numerical methods.

In both Finn & Cox (2001) and Cox & Finn (2007) the fluid flow is quasi-static, with temporal variation in the velocity field only occurring due to changes in domain geometry.

While the above works demonstrate the strong effect of geometry on rod motion, to our knowledge the effect of geometry on an elliptical cylindrical rod translating and rotating inside an elliptical cylinder has not been previously investigated. Due to the linearity of Stokes equations, the velocity field resulting from any prescribed translational motion (in any bounded or unbounded two or three-dimensional domain) can be calculated by considering component motions directed along orthogonal axes and summing the component solutions. The velocity field resulting from prescribed rotational motion in these domains can also be considered separately, and for combined translational and rotational motions the solution is obtained by adding the relative contributions. By implementing the Lorentz reciprocal theorem, it can be shown that the magnitudes of the hydrodynamic forces and torques on a particle moving in Stokes flow vary linearly with the imposed translational and rotational velocities, respectively, and these relationships can be captured by the coefficients of two symmetric *resistance tensors* (Brenner 1962*c*, 1963; Hinch 1972). An additional tensor characterises the interactions between translation and rotation that can occur when particle or domain symmetry is broken (Brenner 1963; Hinch 1972). The general theory for the effect of finite domain boundaries on the resistance tensors has been considered for the case where the particle is small in comparison to its distance from the boundary (Brenner 1962*a,b*). In two-dimensions, the three resistance tensors can be formulated as a single *resistance matrix*. To illustrate this, consider a Cartesian coordinate system with orthogonal directions \mathbf{i} , \mathbf{j} , and \mathbf{k} . For a given prescribed translational velocity, $dx/dt \mathbf{i} + dy/dt \mathbf{j}$, and a prescribed angular velocity $d\theta/dt \mathbf{k}$, the resistance matrix provides the hydrodynamic forces $F_x \mathbf{i}$, $F_y \mathbf{j}$ and hydrodynamic torque $\tau_z \mathbf{k}$ via

$$\begin{bmatrix} F_x \\ F_y \\ \tau_z \end{bmatrix} = - \begin{bmatrix} K_{xx} & K_{xy} & C_x \\ K_{xy} & K_{yy} & C_y \\ C_x & C_y & A_{zz} \end{bmatrix} \begin{bmatrix} dx/dt \\ dy/dt \\ d\theta/dt \end{bmatrix}. \quad (1.1)$$

The scalar matrix coefficients K_{ij} for $i, j = x, y$ in equation (1.1) characterise the resistive force in the i -direction due to motion in the j -direction, and equivalently, as the matrix is symmetric, the resistance in the j -direction due to motion in the i -direction. Coefficient A_{zz} provides the linear relationship between a rotational motion in the cross-section and the resistive torque. Finally, coefficients C_x and C_y describe the coupling between translational and rotational motions, i.e., the rotation induced by translation (and vice versa). The coefficients are all functions of the geometry of the domain. When considering translation without rotation, equation (1.1) reduces to

$$\begin{bmatrix} F_x \\ F_y \end{bmatrix} = - \begin{bmatrix} K_{xx} & K_{xy} \\ K_{xy} & K_{yy} \end{bmatrix} \begin{bmatrix} dx/dt \\ dy/dt \end{bmatrix}. \quad (1.2)$$

The eigenvectors and corresponding eigenvalues of the matrix in equation (1.2) are the directions and magnitudes of the minimum and maximum resistance, respectively. Using principles of energy dissipation, it can be shown that the eigenvalues must be positive. This is proved for a three-dimensional particle of arbitrary shape moving in Stokes flow in Brenner (1962*c*).

As a simple example of the resistance matrix for two dimensional flows, consider the case of concentric circles of inner radius b and outer radius a . Stokes equations can be solved analytically in this geometry for prescribed translational and rotational velocities

of the rod (Slezkin 1955). The resulting (dimensionless) resistance matrix components are

$$K_{xy} = C_x = C_y = 0, \quad (1.3a)$$

$$K_{xx} = K_{yy} = 4\pi(1+r^2)/(1-r^2+(1+r^2)\log r), \quad (1.3b)$$

$$A_{zz} = 4\pi/(1-(1/r)^2), \quad (1.3c)$$

where $r = a/b$. Due to the symmetry of the domain there is no coupling between translation and rotation. Moreover, the two eigenvalues of the matrix in equation (1.2) are given by $K_{xx} = K_{yy}$, i.e. there is equivalent resistance in all directions such that both the translational and rotational resistance decreases monotonically as the ratio r increases. A resistance matrix of the form given in equation (1.1) has been used to describe the motion of a cylindrical rod of circular cross-section translating and rotating in Stokes flow between parallel plates (Dvinsky & Popel 1987). More recently, resistance matrices have been used to understand the interactions between swimming micro-organisms (Ishikawa *et al.* 2006) and to control the movement of aqueous particles (Btait *et al.* 2019).

1.3. Paper summary

This paper is organised as follows. In Section 2 we describe the model set-up. In the regime in which both the aspect ratio of the cylinders and the reduced Reynolds number are small, we show that at leading order the axial and cross-sectional flows can be decoupled into Poiseuille flow and Stokes flow, respectively. In Section 3 we solve the axial flow equations and compute the flux for a given pressure drop as a function of rod position and the cross-sectional shapes of the rod and bounding cylinder. We then determine an optimal configuration that minimises the axial flow resistance. In Section 4 we solve the cross-sectional Stokes flow equations and calculate the forces and torque exerted on the rod by the surrounding viscous fluid when the rod undergoes a prescribed motion. We calculate the resistance matrix coefficients as functions of cross-sectional geometry and determine which configurations are most stable to perturbations in the rod position as follows. For a given instantaneous velocity, it will require the least work to perturb the position of the rod in the direction of minimum resistance. Thus, we define the most stable configuration as the one which maximises the minimum resistance. For circles in ellipses and for ellipses in ellipses of the same eccentricity and orientation, we find that the position of the rod that maximises the axial flow rate is also the most stable position. In Section 5 we turn to rod trajectories of an elliptical rod inside an elliptical cylinder of the same eccentricity, starting from a position where the axes are aligned, assuming that the motion of the rod is subject to an initial instantaneous prescribed velocity in the direction of minimum resistance. As the rod moves through the domain, we allow the relative orientation of the two ellipses to change and we also compute the corresponding axial flow rate, assuming a fixed axial pressure-drop. We show that the axial flow rate increases as a function of time, which demonstrates that the axial flow rate for ellipses in ellipses might increase naturally if the inner ellipse is free to move. Finally, in Section 6, we extend our consideration of optimal axial flow to the full geometric parameter space of an elliptical rod in an elliptical cylinder with fixed area available for the fluid. We conclude in Section 7.

Description	Example Geometry	Poiseuille flow	Stokes flow (rotation)	Stokes flow (translation)
Centred circle in circle		Lamb (1916)	Lamb (1916)	Frazer (1926); Chwang & Wu (1975)
Offset circle in circle		Heyda (1959); Sastry (1964); Redberger (1962); Ebrahim et al. (2013); Snyder & Goldstein (1965); Shivakumar & Chuanxiang (1993)	Jeffrey (1922); Jeffrey & Onishi (1981); Wannier (1950); Slezkin (1955); Finn & Cox (2001)	Finn & Cox (2001)
Fully offset circle in circle		MacDonald (1982)	N/A	N/A
Centred circle in ellipse		Sastry (1964); Shivakumar (1973)		
Offset circle in ellipse			Hackborn (1991) (rod of infinitesimal radius)	
Centred ellipse in circle				
Centred ellipse in ellipse		Sastry (1964) (confocal ellipses)	Saatdjian et al. (1994) (confocal ellipses)	
Offset ellipse in circle			Cox & Finn (2007) (including multiple ellipse case)	Cox & Finn (2007) (including multiple ellipse case)
Offset ellipse in ellipse				
Circle between parallel plates		N/A	Dvinsky & Popel (1987); Yang et al. (2013)	Dvinsky & Popel (1987)

Table 2: Summary of existing literature for relevant geometries.

2. Mathematical model

We consider an inner cylindrical rod which is free to move within a fluid-filled outer cylinder. The rod is prescribed a small, instantaneous, translational motion in a direction perpendicular to, and a rotation about, its longitudinal axis. The subsequent motion of

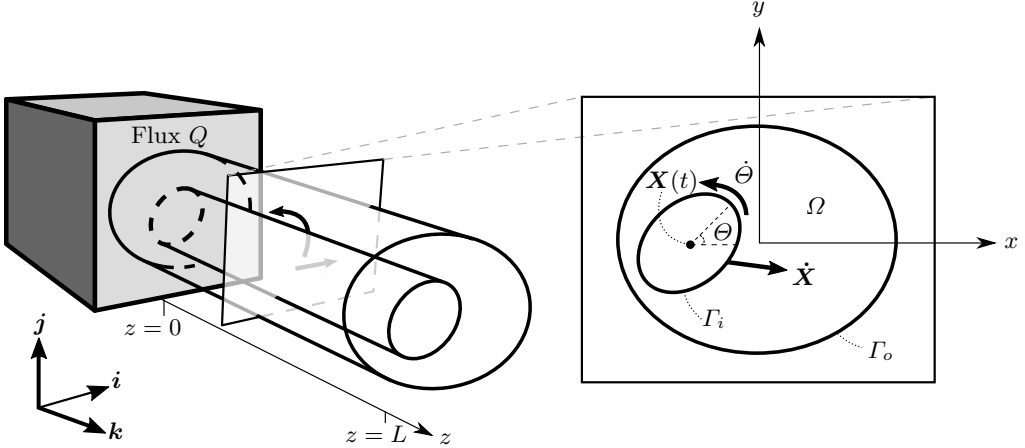


Figure 2: A schematic of the set-up in a Cartesian coordinate system (x, y, z) with corresponding coordinate directions $\mathbf{i}, \mathbf{j}, \mathbf{k}$, where \mathbf{k} is oriented along the common axis of the cylinders of length L . At $z = 0$ the flow is driven by a flux, Q . The boundaries of a cross-sectional slice of the cylinders are denoted Γ_i (inner) and Γ_o (outer), and the fluid-filled area between them is Ω . The inset figure shows a cross-sectional slice, where the position and orientation of the rod are given by \mathbf{X} and Θ , respectively. The rod has translational velocity $\dot{\mathbf{X}}$ and angular velocity $\dot{\Theta}$.

the rod is driven by the hydrodynamic forces exerted on the rod by the fluid. As the rod moves, we assume that it remains coaxial with the outer cylinder. While the rod is able to move in the direction perpendicular to its longitudinal axis, we assume that it does not move axially. It is also able to rotate about its longitudinal axis. Both the translational and angular velocities of the inner rod are constant along its length.

Both cylinders are of length L and have uniform elliptical cross-sections. The space between the inner and outer cylinders is filled with an incompressible, Newtonian fluid of viscosity μ and density ρ . Flow is driven by both an applied non-zero constant axial flux and the motion of the cylindrical rod. We adopt a Cartesian coordinate system (x, y, z) with corresponding coordinate directions $\mathbf{i}, \mathbf{j}, \mathbf{k}$, where \mathbf{k} is oriented along the common axis of the cylinders and $z = 0$ is at the entrance to the annular region (See Figure 2). With subscripts i and o denoting the inner and outer cylinders, respectively, we take the characteristic radii of the cylinders to be

$$R_i = \sqrt{A_i/\pi}, \quad R_o = \sqrt{A_o/\pi}, \quad (2.1a,b)$$

where A_i and A_o are the respective cross-sectional areas. We assume that R_i and R_o are comparable and much smaller than L . We denote the annular boundaries of a cross-sectional slice of the cylinders as Γ_o and Γ_i , respectively. The coordinate position of the geometric centre of the inner rod is given by $(X(t), Y(t), L/2)$, where X and Y are functions of time, and thus the position of the inner rod within the cross-section is $\mathbf{X}(t) = (X(t), Y(t))$. The orientation of the major axis of the rod's cross-section, with respect to the x -axis, is given by $\Theta(t)$, also a function of time (Figure 2).

As motivated in Section 1, we are interested in a regime where fluid inertia is negligible. Thus, the fluid flow is governed by the Stokes and continuity equations

$$-\nabla p + \mu \nabla^2 \mathbf{u} = 0, \quad \nabla \cdot \mathbf{u} = 0, \quad (2.2a,b)$$

where $\mathbf{u} = u \mathbf{i} + v \mathbf{j} + w \mathbf{k}$ and p represent the fluid velocity and pressure, respectively.

A non-zero constant flux, Q , is applied at $z = 0$. Continuity then implies that for all z ,

$$\iint_{\Omega} \mathbf{u} \cdot \mathbf{k} \, d\Omega = Q, \quad (2.3)$$

where Ω is the 2D region of the cross-section between the cylinders. No-slip conditions at the surfaces of the inner and outer cylinder give

$$\left. \begin{array}{l} u = \dot{X} - \dot{\Theta}(y - Y), \\ v = \dot{Y} + \dot{\Theta}(x - X), \\ w = 0, \end{array} \right\} \quad \text{on } \Gamma_i \quad (2.4a-c)$$

and

$$\mathbf{u} = \mathbf{0}, \quad \text{on } \Gamma_o, \quad (2.5)$$

respectively. To calculate $\dot{\mathbf{X}}$ and $\dot{\Theta}$, where dots denote derivatives with respect to time, we consider conservation of linear and angular momentum for the inner rod which gives

$$m\ddot{\mathbf{X}} = \mathbf{F}(\mathbf{X}, \Theta, \dot{\mathbf{X}}, \dot{\Theta}, \mu, L), \quad I\ddot{\Theta} = \tau(\mathbf{X}, \Theta, \dot{\mathbf{X}}, \dot{\Theta}, \mu, L), \quad (2.6a,b)$$

where m and I are the rod mass and the moment of inertia about the rod axis, respectively, and \mathbf{F} and τ are the hydrodynamic force in the cross-section and z -component of the torque exerted on the rod due to the motion of the fluid. Because the cylinders remain coaxial, τ and \mathbf{F} are the only non-zero force and torque components.

The force and torque are calculated using

$$\mathbf{F} = \int_0^L \left[\oint_{\Gamma_i} \boldsymbol{\sigma} \mathbf{n}_i \, ds \right] dz, \quad (2.7a)$$

$$\tau = \int_0^L \left[\oint_{\Gamma_i} (x - X)(\boldsymbol{\sigma} \mathbf{n}_i) \cdot \mathbf{j} - (y - Y)(\boldsymbol{\sigma} \mathbf{n}_i) \cdot \mathbf{i} \, ds \right] dz, \quad (2.7b)$$

where $\boldsymbol{\sigma}$ is the two-dimensional stress tensor for the fluid, and \mathbf{n}_i is the unit outward normal to Γ_i . The stress tensor is given by

$$\boldsymbol{\sigma} = [-p \mathbf{I} + \mu(\nabla \mathbf{u}^\perp + (\nabla \mathbf{u}^\perp)^T)], \quad (2.8)$$

where \mathbf{I} is the two-dimensional identity matrix, $\nabla_\perp = \partial/\partial x \mathbf{i} + \partial/\partial y \mathbf{j}$, and $\mathbf{u}^\perp = u \mathbf{i} + v \mathbf{j}$. As initial conditions for equations (2.6) we prescribe

$$\mathbf{X}(0) = \mathbf{X}_0, \quad \Theta(0) = \Phi_0, \quad \dot{\mathbf{X}}(0) = U \ell, \quad \dot{\Theta}(0) = \omega_0, \quad (2.9a-d)$$

where \mathbf{X}_0 is the initial location of the rod's axis in the (x, y) plane, Φ_0 is its initial orientation angle, U is its initial velocity in a direction given by ℓ , a unit vector in the (x, y) -plane, and ω_0 is its initial angular velocity about the z -axis.

2.1. Non-dimensionalisation

We define the aspect ratio of the rod to be

$$\epsilon = R_i/L \ll 1, \quad (2.10)$$

and the axial velocity scale, W , to be

$$W = Q/R_i^2. \quad (2.11)$$

We then non-dimensionalise as follows

$$(x, y, z) = L(\epsilon \hat{x}, \epsilon \hat{y}, \hat{z}), \quad \mathbf{X} = \epsilon L \hat{\mathbf{X}}, \quad t = (L/W)\hat{t}, \quad (2.12a-c)$$

$$p = (W\mu/L\epsilon^2)\hat{p}, \quad (u, v, w) = W(\epsilon \hat{u}, \epsilon \hat{v}, \hat{w}), \quad (2.12d,e)$$

$$\mathbf{F} = \epsilon L \mu W \hat{\mathbf{F}}, \quad \tau = \epsilon^2 L^2 \mu W \hat{\tau}, \quad (2.12f,g)$$

where hats denote dimensionless quantities. The scaling for pressure is chosen to balance the viscous terms in equation (2.2), and the time-scale is set by the advection of the fluid along the cylinder. We also scale the parameters in the initial conditions (2.9)

$$\hat{U} = U/\epsilon W, \quad \hat{\omega} = \omega L/W, \quad \hat{\boldsymbol{\chi}} = \boldsymbol{\chi}/\epsilon L, \quad (2.13a-c)$$

which we assume are all $\mathcal{O}(1)$, i.e., the initial imposed rod velocities are ϵ times smaller than the axial velocity. The rod has a unit dimensionless characteristic radius and we define the characteristic radius of the outer cylinder to be

$$\hat{R}_o = R_o/R_i. \quad (2.14)$$

Henceforth we will refer to dimensionless quantities, dropping the hat notation. The dimensionless forms of equations (2.2) are given in component form by

$$-p_x + \epsilon^2(u_{xx} + u_{yy}) + \epsilon^4 u_{zz} = 0, \quad (2.15a)$$

$$-p_y + \epsilon^2(v_{xx} + v_{yy}) + \epsilon^4 v_{zz} = 0, \quad (2.15b)$$

$$-p_z + w_{xx} + w_{yy} + \epsilon^2 w_{zz} = 0, \quad (2.15c)$$

$$u_x + v_y + w_z = 0, \quad (2.15d)$$

where we have adopted the subscript notation for partial derivatives. Due to the scaling for velocity, equation (2.11), the flux scales to

$$Q = 1. \quad (2.16)$$

The dimensionless boundary conditions (2.4), and (2.5) are

$$\left. \begin{aligned} u &= \dot{X} - \dot{\Theta}(y - Y), \\ v &= \dot{Y} + \dot{\Theta}(x - X), \\ w &= 0, \end{aligned} \right\} \quad \text{on } \Gamma_i \quad (2.17a-c)$$

and

$$\mathbf{u} = \mathbf{0}, \quad \text{on } \Gamma_o. \quad (2.18)$$

The dimensionless forms of equations (2.6) are

$$\ddot{\mathbf{X}} = \alpha \mathbf{F}(\mathbf{X}, \Theta, \dot{\mathbf{X}}, \dot{\Theta}), \quad \ddot{\Theta} = \alpha' \tau(\mathbf{X}, \Theta, \dot{\mathbf{X}}, \dot{\Theta}), \quad (2.19a,b)$$

where

$$\alpha = \mu L^2/mW, \quad \alpha' = R_i^2 \mu L^2/IW, \quad (2.20a,b)$$

and α' is the same size as α as I scales with $R_i^2 m$. We note that α can be rearranged to relate the fluid density to the material density of the inner rod multiplied by the reduced Reynolds number. As discussed in the introduction, we will consider the regime where this parameter is $\mathcal{O}(1)$. The dimensionless initial conditions, equations (2.9), are

$$\mathbf{X}(0) = \mathbf{X}, \quad \Theta(0) = \Phi, \quad \dot{\mathbf{X}}(0) = U\boldsymbol{\ell}, \quad \dot{\Theta}(0) = \omega, \quad (2.21a-d)$$

2.2. Asymptotic analysis

We take $\epsilon^2 \ll 1$ and seek expansions to our dimensionless variables of the forms

$$\mathbf{u} = \mathbf{u}_0 + \epsilon^2 \mathbf{u}_1 + \dots, \quad p = p_0 + \epsilon^2 p_1 + \dots \quad (2.22a,b)$$

$$\mathbf{X} = \mathbf{X}_0 + \epsilon^2 \mathbf{X}_1 + \dots, \quad \Theta = \Theta_0 + \epsilon^2 \Theta_1 + \dots \quad (2.22c,d)$$

Inserting (2.22a,b) into equations (2.15c), (2.15d) and equating $\mathcal{O}(1)$ terms gives

$$\nabla_{\perp}^2 w_0 = \frac{dp_0}{dz}, \quad \nabla_{\perp} \cdot \mathbf{u}_0^{\perp} + w_{0z} = 0, \quad (2.23a,b)$$

where $\mathbf{u}_0^{\perp} = u_0 \mathbf{i} + v_0 \mathbf{j}$. To determine the cross-sectional velocity components, u_0 and v_0 , we consider equations (2.15a) and (2.15b) at $\mathcal{O}(\epsilon^2)$, and obtain the two-dimensional Stokes equations

$$\nabla_{\perp}^2 u_0 = p_{1x}, \quad \nabla_{\perp}^2 v_0 = p_{1y}. \quad (2.24a,b)$$

The leading-order flux condition is

$$\iint_{\Omega} w_0 \, d\Omega = 1, \quad (2.25)$$

and leading-order boundary conditions are

$$\left. \begin{aligned} u_0 &= \dot{X}_0 - \dot{\Theta}_0(y - Y_0), \\ v_0 &= \dot{Y}_0 + \dot{\Theta}_0(x - X_0), \\ w_0 &= 0, \end{aligned} \right\} \quad \text{on } \Gamma_i \quad (2.26a-c)$$

and

$$\mathbf{u}_0^{\perp} = \mathbf{0} \text{ and } w_0 = 0, \quad \text{on } \Gamma_o. \quad (2.27a,b)$$

The equations of motion for the tool, (2.19), read at leading order

$$\ddot{\mathbf{X}}_0 = \alpha \mathbf{F}_0(\mathbf{X}_0, \Theta_0, \dot{\mathbf{X}}_0, \dot{\Theta}_0), \quad \ddot{\Theta}_0 = \alpha' \tau_0(\mathbf{X}_0, \Theta_0, \dot{\mathbf{X}}_0, \dot{\Theta}_0), \quad (2.28a,b)$$

where

$$\mathbf{F}_0 = \int_0^1 \left[\oint_{\Gamma_i} \boldsymbol{\sigma}_0 \mathbf{n}_i \, ds \right] dz, \quad (2.29a)$$

$$\tau_0 = \int_0^1 \left[\oint_{\Gamma_i} (x - X_0)(\boldsymbol{\sigma}_0 \mathbf{n}_i) \cdot \mathbf{j} - (y - Y_0)(\boldsymbol{\sigma}_0 \mathbf{n}_i) \cdot \mathbf{i} \, ds \right] dz, \quad (2.29b)$$

for

$$\boldsymbol{\sigma}_0 = [-(p_0/\epsilon^2 + p_1)\mathbf{I} + (\nabla \mathbf{u}_0^{\perp} + \nabla \mathbf{u}_0^{\perp})^T]. \quad (2.30)$$

The leading-order initial conditions for the rod motion are

$$\mathbf{X}_0(0) = \mathbf{x}, \quad \Theta_0(0) = \Phi, \quad \dot{\mathbf{X}}(0) = \mathbf{U}, \quad \dot{\Theta} = \omega. \quad (2.31)$$

We seek a separable solution for w_0 of the form

$$w_0 = f(x, y) \frac{dp_0}{dz}. \quad (2.32)$$

Integrating equation (2.23b) over a cross-section of the fluid domain between the two cylinders, using equations (2.26) and (2.27), and applying the divergence theorem gives

$$w_{0z} = 0, \quad (2.33)$$

so that dp_0/dz is a constant. Hence equation (2.23b) becomes

$$\nabla_{\perp} \cdot \mathbf{u}_0^{\perp} = 0, \quad (2.34)$$

and the governing equation for the axial fluid flow, (2.23a), is

$$\nabla_{\perp}^2 f(x, y) = 1, \quad (2.35)$$

with no-slip boundary conditions, equations (2.26c) and (2.27b),

$$f = 0, \text{ on } \Gamma_i, \Gamma_o. \quad (2.36)$$

Additionally, using (2.16) we can solve for the constant pressure gradient

$$\frac{dp_0}{dz} = \left[\iint_{\Omega} f(x, y) d\Omega \right]^{-1}, \quad (2.37)$$

and thus

$$w_0 = f(x, y) \left[\iint_{\Omega} f(x, y) d\Omega \right]^{-1}, \quad (2.38)$$

combining (2.32) and (2.37).

As p_0 is constant within a cross-section it has no contribution to the leading-order hydrodynamic force and torque given by equations (2.29). Additionally, the bracketed terms in equations (2.29) are independent of z , and hence equations (2.29) and (2.30) to calculate the force and torque reduce to

$$\mathbf{F}_0 = \oint_{\Gamma_i} \boldsymbol{\sigma}_0 \mathbf{n}_i ds, \quad (2.39a)$$

$$\tau_0 = \oint_{\Gamma_i} (x - X_0)(\boldsymbol{\sigma}_0 \mathbf{n}_i) \cdot \mathbf{j} - (y - Y_0)(\boldsymbol{\sigma}_0 \mathbf{n}_i) \cdot \mathbf{i} ds, \quad (2.39b)$$

for

$$\boldsymbol{\sigma}_0 = [-p_1 \mathbf{I} + (\nabla \mathbf{u}_0^{\perp} + \nabla \mathbf{u}_0^{\perp})^T]. \quad (2.40)$$

Henceforth, we will drop leading-order subscripts. We will retain the subscript on the only first-order term that appears in our leading-order system, p_1 , to differentiate the first-order pressure that drives flow in the cross-section, equations (2.24), from the leading-order pressure that drives the axial flow, equation (2.23a).

2.3. Model summary and computational approach

Equations (2.35), (2.36), and (2.38) give rise to Poiseuille-flow, where the axial flow resistance, $\mathcal{R}(\mathbf{X}, \Theta)$, is equal to the constant pressure gradient required to maintain the axial flow through the annular domain at unit flux. This is given by

$$\mathcal{R}(\mathbf{X}, \Theta) = \left[\iint_{\Omega} f(x, y) d\Omega \right]^{-1}, \quad (2.41)$$

a function of domain geometry. We note that for any given flux,

$$Q = \frac{1}{\mathcal{R}(\mathbf{X}, \Theta)} \frac{dp}{dz}, \quad (2.42)$$

and so, once $\mathcal{R}(\mathbf{X}, \Theta)$ is determined via equation (2.41), we can compute $Q(\mathbf{X}, \Theta)$ for any specified pressure gradient. Motivated by the urological application, in which it is most natural to consider optimising flow rate for a given pressure drop, our approach in Sections 3 and 6 will be to fix $dp/dz = 1$ as a model input and compute $Q(\mathbf{X}, \Theta)$ and the associated flow profile as primary outputs. In this view, minimising the resistance is equivalent to maximising the flux.

The equations governing the cross-sectional flow are the Stokes equations (2.24) and incompressibility (2.34), with no-slip boundary conditions (2.26a,b) and (2.27a). As discussed in Section 1, the forces and torque on the inner rod, equations (2.39a,b), are linearly related to the imposed velocities via resistance coefficients

$$\mathbf{F}(\mathbf{X}, \Theta, \dot{\mathbf{X}}, \dot{\Theta}, \mu, L) = -[\mathbf{K}(\mathbf{X}, \Theta)\dot{\mathbf{X}} + \mathbf{C}(\mathbf{X}, \Theta)\dot{\Theta}], \quad (2.43a)$$

$$\tau(\mathbf{X}, \Theta, \dot{\mathbf{X}}, \dot{\Theta}, \mu, L) = -[A_{zz}(\mathbf{X}, \Theta)\dot{\Theta} + C_x(\mathbf{X}, \Theta)\dot{X} + C_y(\mathbf{X}, \Theta)\dot{Y}], \quad (2.43b)$$

where $\mathbf{K}(\mathbf{X}, \Theta)$ is the two dimensional translation matrix and $\mathbf{C}(\mathbf{X}, \Theta)$ describes the coupling between translation and rotation

$$\mathbf{K}(\mathbf{X}, \Theta) = \begin{bmatrix} K_{xx} & K_{xy} \\ K_{xy} & K_{yy} \end{bmatrix}, \quad \mathbf{C}(\mathbf{X}, \Theta) = \begin{bmatrix} C_x \\ C_y \end{bmatrix}. \quad (2.44a,b)$$

The resistance coefficients in equations (2.44a,b) are also functions of domain geometry. We will compute these in Section 4. To explore the effect of geometry on both the axial and cross-sectional resistances we consider configurations I), II), and III), as introduced in Section 1. In each configuration, we will fix the cross-sectional areas of the cylinders to constrain the space available for fluid. This reduces the parameter space, allowing for full interrogation of the axial and transverse flows on \mathbf{X} , Θ , and the shape of the elliptical cross-sections of the inner and outer cylinders. The governing equations for the fluid flow (2.35), (2.24), and (2.34) are quasi-static, with time entering only via the time-dependence of the rod position, $\mathbf{X} = (X, Y)$ and orientation Θ . In Sections 3 and 4 we restrict to static calculations, computing the axial resistance for a fixed position of inner rod, and the instantaneous resistance to cross-sectional motion. In Section 5 we then compute rod trajectories by solving the equations of motion (2.28) while (quasi-statically) updating the cross-sectional fluid velocities. In this approach we can also monitor changes to the associated instantaneous axial flow. Section 6 returns to the static calculation and considers a more complete optimization problem in which we relax our previous restrictions on the considered elliptical geometries.

3. Axial flow

We begin by considering the effect of cross-sectional geometry on axial flow by solving equation (2.35) subject to conditions (2.36) for varying ellipse cross-sectional geometries. Results were calculated numerically using an open-source finite element library, **oomph-lib** (Heil & Hazel 2006). However, in Section 3.3, when we consider the cylinders' cross-sections to be of the same eccentricity and orientation, we also utilised a Bipolar coordinate transformation to map the annular geometry to a rectangular domain and solve the transformed equations and boundary conditions using a finite difference method. This alternative approach enabled us to validate the finite element solutions (discussed in more detail in Appendix B).

Our objective is to explore how the flux is affected by the position and orientation of the inner rod, \mathbf{X} and Θ , respectively, and the elliptical eccentricity of the cross-sections. The eccentricity is defined as

$$e_{i,o} = \sqrt{1 - (b_{i,o}/a_{i,o})^2}, \quad (3.1)$$

where $a_{i,o}$ and $b_{i,o}$ are the major and minor axes of the inner and outer cylinder, respectively. A zero eccentricity value therefore corresponds to a circle and $e = 1$ is a slit of zero width and infinite length. For fixed characteristic radii, see equations (2.1), and given eccentricity, $e_{i,o}$, we can calculate $a_{i,o}$ and $b_{i,o}$

$$a_i = (1 - e_i^2)^{-1/4}, \quad b_i = (1 - e_i^2)^{1/4}, \quad (3.2a,b)$$

$$a_o = R_o(1 - e_o^2)^{-1/4}, \quad b_o = R_o(1 - e_o^2)^{1/4}, \quad (3.2c,d)$$

3.1. I) Circle in ellipse

In Figure 3 we consider a circular rod (of dimensionless unit radius) inside a cylinder of elliptical cross-section (with characteristic radius $R_o = 2$). We vary the eccentricity of the outer cylinder's cross-section while maintaining the cross-sectional area, using equations (3.2) to determine the corresponding lengths of the major and minor axes. When, for each value of e_o , the rod is located at the position that maximises flux (see Appendix A), we find that the flux initially increases with e_o . The maximum flux over all e_o (data point (ii)) is nearly 50% higher than the flux for a circular outer cylinder of the same cross-sectional area (data point (i)). The eccentricity at which the maximum flux is achieved is $e_o \approx 0.84$ for $R_o = 2$. We might hypothesise that this coincides with the value for e_o where the rod and bounding cylinder match curvature at the cylinder's vertex, which we denote e^* (Appendix A). However, for $R_o = 2$, $e^* \approx 0.78$, which is less than the e_o value where maximum flux is achieved. In fact, in configuration (ii) in Figure 3, although hard to discern from the colourmap, the circular rod tangentially touches the elliptic cylinder in two locations. The colorbars in Figure 3 give the magnitude of the axial velocity, and demonstrate that the maximum velocity within the cross-section is also larger in configuration (ii), than in either (i) and (iii).

3.2. II) Ellipse in circle

We next consider an elliptical inner rod and circular outer rod ($e_o = 0$). We take $R_o = 3$ and vary \mathbf{X} , Θ_0 , and e_i . Due to the rotational symmetry of the outer cylinder, we can, without loss of generality, fix $\mathbf{X} = (X, 0)$ and vary the inner rod's position along the x -axis only. Here there is more available space for the fluid than in the previous section as we have taken $R_o = 3$ rather than $R_o = 2$; this is to allow elliptical rods to

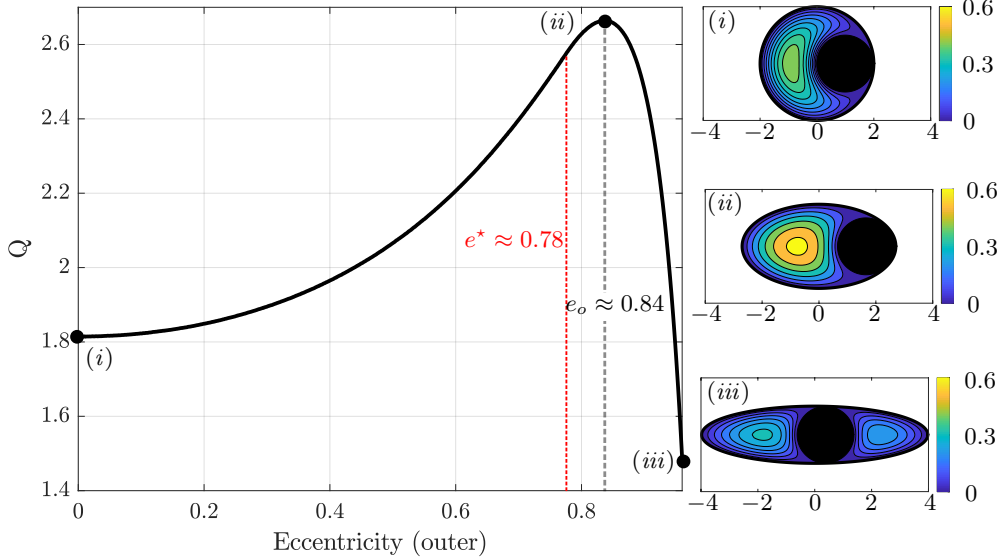


Figure 3: Dimensionless flow rate, \mathcal{Q} , as a function of e_o , for a circle of unit radius inside an ellipse of characteristic radius $R_o = 2$. The eccentricity is changed while maintaining the cross-sectional area. For each e_o the inner circle is located at the position that maximises the axial flux (see Appendix A). When $e = e^*$, the ellipse matches curvature with the circle at the ellipse vertex. The colorbars provide the magnitude of the axial velocity.

fit in the cross-section at a wider range of positions and orientations. The flux is plotted in Figure 4 for all combinations of $e_i = 0$, $e_i = 0.7$, $e_i = 0.9$, and $\Theta = 0$, $\Theta = \pi/4$, and $\Theta = \pi/2$. For a circular rod ($e_i = 0$), we validate our numerical solution against the analytical solution for offset circles (Heyda 1959)* in addition to confirming that our numerical solution approaches the limiting case of touching circles (MacDonald 1982) as X approaches 2. We note that, although it appears from Figure 4 (a)-(c) that the maximum flux is achieved for a rod of circular cross-section, this is because we have presented \mathcal{Q} as a function of X . For the elliptical rods in Figures 4 (b) and (c) to fit inside the domain when $\Theta = 0$, they must be further from the edge of the bounding cylinder. Allowing the rod to move closer to the wall when the geometry permits, we obtain the largest flux, for the configurations considered, when $e_i = 0.9$ and $\Theta = \pi/2$ (Figure 4d). When the rod is centred in the outer cylinder ($X = 0$) the flux is independent of Θ due to the geometry of the domain. The largest flux for a rod centred in a circular cylinder of radius $R_o = 3$ is obtained when the rod is circular, and decreases with e_i . A zoom-in on the region $0 \leq X \leq 0.2$ for $e_i = 0$, $e_i = 0.7$, and $e_i = 0.9$ oriented at $\pi/2$ is shown in the inset of Figure 4d, illustrating that the increased eccentricity only generates an increased flux if there is sufficient offset.

3.3. III) Ellipse in ellipse

We now consider cylinders with elliptical cross-sections of the same eccentricities (given by equation (3.1)) and orientation ($\Theta = 0$). We fix $R_o = 2$ and again seek configurations that maximise the flux. In Section 6 we will address the question of global flux optimality,

*As Heyda (1959) presents a solution for the velocity field in terms of an infinite sum, we truncate this sum and integrate numerically to determine the flow rate.

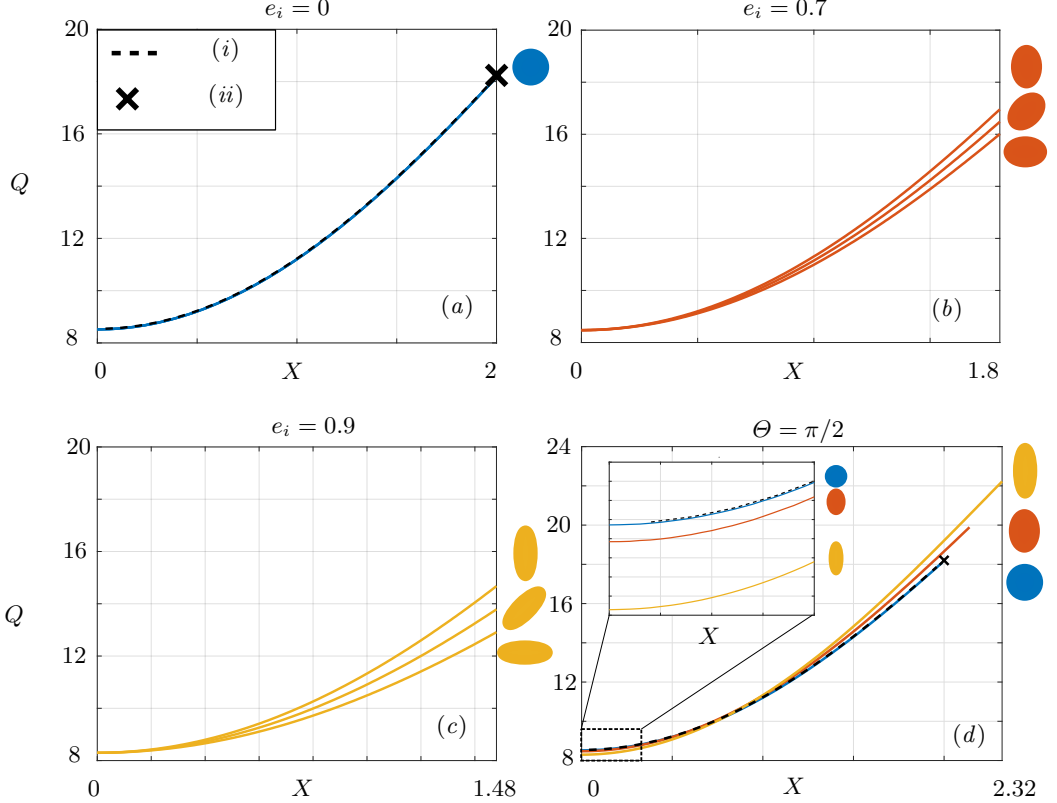


Figure 4: Dimensionless flow rate, Q , as a function of X for an ellipse of characteristic radius of $R_o = 3$. We vary the eccentricity of the inner ellipse (a) $e_i = 0$, (b) $e_i = 0.7$, (c) $e_i = 0.9$. In plots (a)-(c), three orientations $\Theta = 0, \pi/4$, and $\pi/2$ are presented. (d) plots Q as a function of X for $e_i = 0$ (blue) $e_i = 0.7$ (red) $e_i = 0.9$ (yellow) oriented at $\pi/2$. The inset plot provides a zoomed-in view from $X = 0$ to $X = 0.2$. In Figures (a) and (d), the solutions of (i) Heyda (1959) and (ii) MacDonald (1982) are included (see Table 2 for more details).

and consider all configurations of ellipses (for fixed cross-sectional areas[†]). Under the constraint that the inner and outer cross-sections have the same elliptical eccentricity and orientation, we can map a domain of non-concentric ellipses to non-concentric circles and formulate the problem in a Bipolar coordinate system (see Appendix B). To describe the position of the inner ellipse relative to the outer ellipse we first define θ to be the angle between the major axis of the outer ellipse and a line connecting the centres of the two ellipses, see Figure 5. The effective radii of the inner and outer ellipses are then defined as

$$r_i = a_i b_i / \sqrt{a_i^2 \sin^2 \theta + b_i^2 \cos^2 \theta}, \quad r_o = a_o b_o / \sqrt{a_o^2 \sin^2 \theta + b_o^2 \cos^2 \theta}. \quad (3.3)$$

[†]It is worthwhile to note, when comparing flux values between different geometries, that in this section and in Section 6, $R_o = 2$, so the space available for fluid flow is the same as in Figure 3 (a circular rod in an elliptical cylinder) but less than in Figure 4 (an elliptical rod in a circular cylinder) where $R_o = 3$.

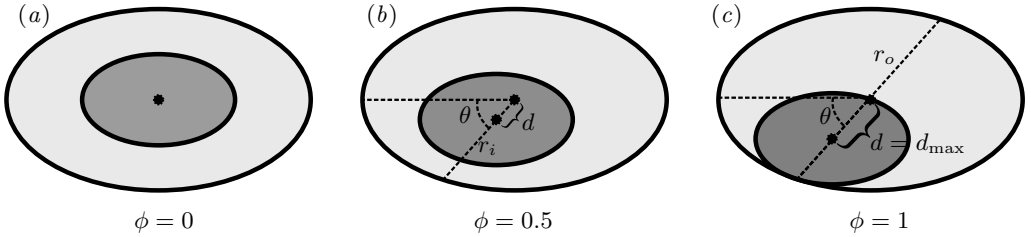


Figure 5: Schematic showing a sample geometry for $e = 0.8$, $\theta = \pi/4$ and (a) $\phi = 0$, (b) $\phi = 0.5$, (c) $\phi = 1$. The shaded ellipse is the cross-section of the rod.

With these definitions, the maximum distance, d_{\max} between the centres at an angle θ (when the rod and the outer cylinder touch) is given by

$$d_{\max} = r_o - r_i. \quad (3.4)$$

From this we define an offset parameter, ϕ , that is the ratio of the distance between the centres of the two ellipses at an angle θ and d_{\max} ,

$$\phi = d/d_{\max}. \quad (3.5)$$

Thus, the domain is characterised by three parameters; the eccentricity, $e \in [0, 1]$, the angle of offset, $\theta \in [0, \pi/2]$, and the relative offset, $\phi \in [0, 1]$ (see Figure 5). We note that when using a Bipolar coordinate system, outlined in Appendix A, $\phi = 1$ is not possible as the coordinate transformation would involve dividing by zero (when the inner ellipse touches the outer boundary). This is purely an artifact of this mathematical technique, and solving the equations with finite elements enables us to consider touching boundaries. However, to use the method in Appendix A for numerical validation, we restrict to the range $\phi \in [0, 0.99]$.

In Figure 6a-d we fix $e = 0.8$ and $\theta = 0$, and plot the velocity profiles (with corresponding flux values indicated) for $\phi = 0.01$, $\phi = 0.35$, $\phi = 0.7$, and $\phi = 0.99$. We observe that Q increases with ϕ , a result previously known for $e = 0$ (Heyda 1959; Redberger 1962). The effects of θ and e on Q are less intuitive. In Figure 6e-h we fix $e = 0.8$ and $\phi = 0.99$ and vary θ , plotting the associated velocity colourmaps for $\theta = 0$, $\theta = \pi/6$, $\theta = \pi/3$, and $\theta = \pi/2$. The flux is largest for $\theta = 0$ and smallest for $\theta = \pi/3$ demonstrating, for the chosen parameters, non-monotonicity of Q with θ . We vary e in Figure 6i-l for fixed $\theta = 0$ and $\phi = 0.99$. The flux is largest for $e = 0.6$ and smallest for $e = 0.9$, also demonstrating, for the chosen parameters, non-monotonicity of Q with e . For completeness, line-plots of Q as a function of independent variation of e , ϕ , and θ can be found in Appendix C.

In Figures 7a-c, we show surface plots of Q in (ϕ, θ) space for three different eccentricities: $e = 0$, $e = 0.7$, and $e = 0.9$, respectively. Note that, as Q varies most significantly with ϕ , we have restricted to $0.9 \leq \phi \leq 0.99$ to isolate the effects of θ and e . When $e = 0$ (Figure 7a), Q is independent of θ due to the rotational symmetry of the domain, and increases monotonically with ϕ . For eccentric domains, $e = 0.7$ and $e = 0.9$ (Figures 7b and c, respectively), Q is minimal at an intermediate value of θ and $\phi = 0.9$ (the smallest value plotted). The maximum Q is seen in Figure 7b for $e = 0.7$, further validating the existence of a nonzero eccentricity value that maximises flux, e^{\max} . This existence of a non-zero eccentricity at which flux is maximised may be of particular interest from an engineering design point of view (Williams *et al.* 2019). However, it is noteworthy that the optimal eccentricity itself will change based on the outer geometry. We plot e^{\max} as a function of R_o in Figure 7d. As $R_o \rightarrow \infty$, $e^{\max} \rightarrow 0$. As R_o characterises the ratio

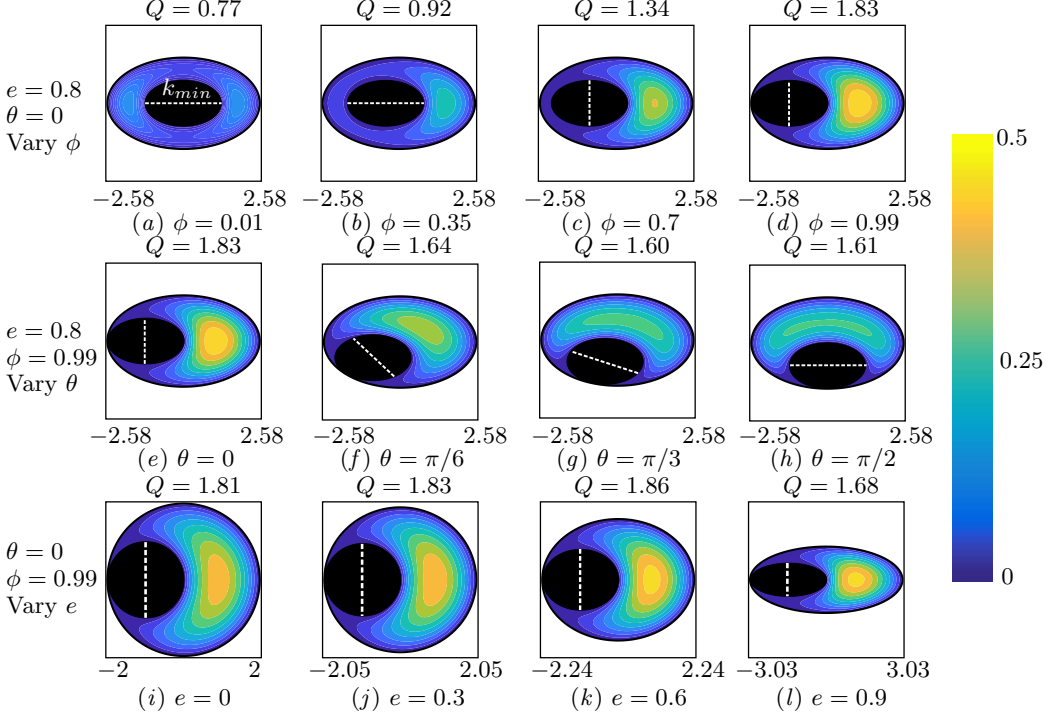


Figure 6: Dimensionless velocity colourmaps with flux values, Q , for ellipses of equal eccentricities and orientations. Here $R_o = 2$. Axes are in (x, y) coordinates and these vary with eccentricity so that the available space for fluid flow is constant. Colourbars reflect different velocity values within the domains. The direction of the axis of minimal resistance, \mathbf{k}_{\min} , is indicated by the dashed white line on each diagram. This will be discussed in Section 4.

Plots (a)-(d) show the effect of offset, ϕ , for $e = 0.8$ and $\theta = 0$. Offset values are (a) $\phi = 0.01$, (b) $\phi = 0.35$, (c) $\phi = 0.7$, and (d) $\phi = 0.99$.

Plots (e)-(h) show the effect of angular position, θ , for $e = 0.8$ and $\phi = 0.99$. Angular position values are (a) $\theta_e = 0$, (b) $\theta = \pi/6$, (c) $\theta = \pi/3$, and (d) $\theta = \pi/2$.

Plots (i)-(l) show the effect of eccentricity, e , for $\phi = 0.99$ and $\theta = 0$. Eccentricity values are (a) $e = 0$, (b) $e = 0.3$, (c) $e = 0.6$, and (d) $e = 0.9$.

between outer and inner cross-sectional areas, the limit as $R_o \rightarrow \infty$ corresponds to a negligible obstruction within the channel, and hence, the maximum flux will be attained for a circular cross-section (Williams *et al.* 2019).

In this section we have determined that for equal eccentricities and orientations of the outer and inner ellipses, there is a position for the inner ellipse and a non-zero eccentricity value that maximises flux. We note that this may not be the configuration that maximises flux for all values of e_i , e_o , X_0 , Y_0 , and Θ_0 , and we consider this global optimisation problem in more detail in Section 6.

4. Cross-sectional flow

We now turn attention to the cross-sectional flow problem, governed by equations (2.24), (2.34), and the no-slip conditions (2.26a,b) and (2.27a). The objective is again to explore the impact of cross-sectional geometry within the configuration space of I) circular rod in elliptical cylinder, II) elliptical rod in circular cylinder, III) elliptical rod

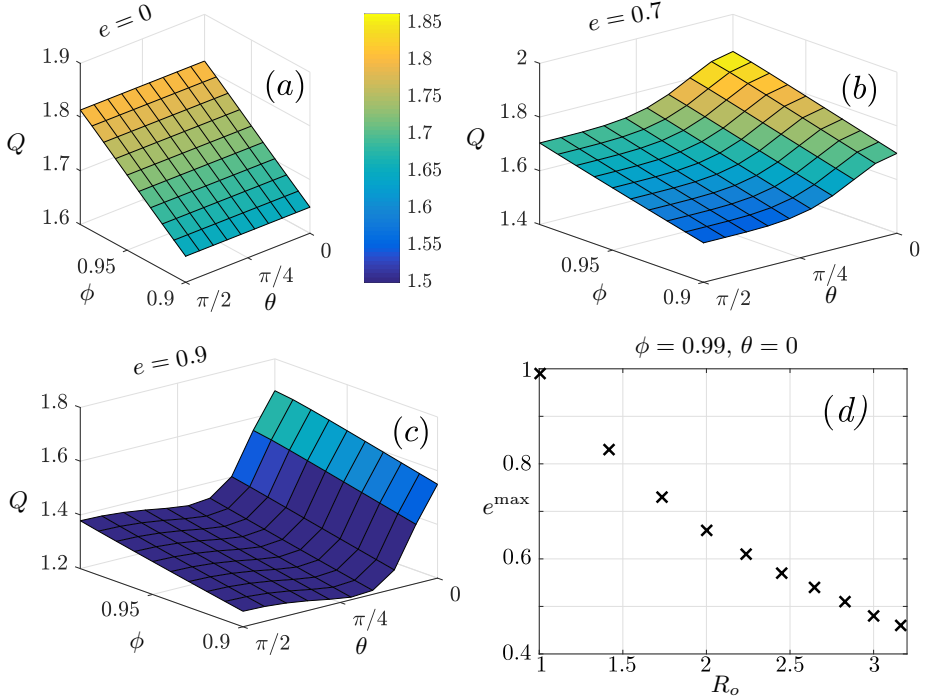


Figure 7: Surface plots (a)-(c) give the dimensionless flow rate, Q , as a function of both offset, ϕ , and angular position θ of the inner ellipse for three different eccentricity values: (a) $e = 0$, (b) $e = 0.7$, and (c) $e = 0.9$. Here $R_o = 2$.

Plot (d) gives e^{\max} as a function of the characteristic radius R_o . The e^{\max} value is calculated as the one that produces maximum flow over 100 values from $0.01 \leq e \leq 0.99$ for each radius ratio.

in elliptical cylinder of same eccentricity and orientation; but here the question is how the geometry impacts the resistance coefficients for cross-sectional rod motion.

We solve the equations numerically using a finite element method implemented in **oomph-lib** (Heil & Hazel 2006), and subsequently compute the dimensionless forces and torques on the rod due to the surrounding fluid via equations (2.39). We validate our numerical solution by comparing with analytical solutions for geometries where these are available in the literature.

We consider a cross-section of the domain illustrated in Figure 2 (i), where the rod is given a prescribed instantaneous velocity, $\dot{\mathbf{X}} = (\dot{X}, \dot{Y})$ in the (x, y) plane and a rotation, $\dot{\Theta}$ about the z -axis. The resulting forces and torques, $\mathbf{F} = (F_x, F_y)$ and τ , are linearly related to (\dot{X}, \dot{Y}) and $\dot{\Theta}$ by a symmetric resistance matrix

$$\begin{bmatrix} F_x \\ F_y \\ \tau_z \end{bmatrix} = - \begin{bmatrix} K_{xx} & K_{xy} & C_x \\ K_{xy} & K_{yy} & C_y \\ C_x & C_y & A_{zz} \end{bmatrix} \begin{bmatrix} \dot{X} \\ \dot{Y} \\ \dot{\Theta} \end{bmatrix}, \quad (4.1)$$

as discussed in Sections 1.2 and 2.3. If $\dot{\Theta} = 0$ then

$$\begin{bmatrix} F_x \\ F_y \end{bmatrix} = - \begin{bmatrix} K_{xx} & K_{xy} \\ K_{xy} & K_{yy} \end{bmatrix} \begin{bmatrix} \dot{X} \\ \dot{Y} \end{bmatrix}. \quad (4.2)$$

The eigenvectors of the 2×2 matrix in equation (4.2) are the directions of minimum and maximum opposing force experienced by the rod due to the flow. We will refer to these as the directions of minimum and maximum resistance. The corresponding eigenvalues give the magnitudes of the opposing forces that result from moving in the directions of minimum and maximum resistance with unit velocity. These values are non-negative (see Section 1.2) and are given by

$$K_{\max} = (1/2) \left(K_{xx} + K_{yy} + \sqrt{(K_{xx} - K_{yy})^2 + 4K_{xy}^2} \right), \quad (4.3a)$$

$$K_{\min} = (1/2) \left(K_{xx} + K_{yy} - \sqrt{(K_{xx} - K_{yy})^2 + 4K_{xy}^2} \right), \quad (4.3b)$$

with corresponding directions of minimum and maximum resistance

$$\mathbf{k}_{\max,\min} = (K_{xy}, K_{\max,\min} - K_{xx}). \quad (4.4)$$

The six unique scalars in the resistance matrix (4.1) can be computed by imposing:

$$\dot{\mathbf{X}} = (1, 0), \quad \dot{\Theta} = 0, \quad \rightarrow \quad K_{xx}, K_{xy} \text{ and } C_x, \quad (4.5a)$$

$$\dot{\mathbf{X}} = (0, 1), \quad \dot{\Theta} = 0, \quad \rightarrow \quad K_{yy}, K_{xy} \text{ and } C_y, \quad (4.5b)$$

$$\dot{\mathbf{X}} = (0, 0), \quad \dot{\Theta} = 1, \quad \rightarrow \quad C_x, C_y \text{ and } A_{zz}, \quad (4.5c)$$

where each calculation provides us with the coefficients indicated by the arrows. We note that K_{xy} , C_x , and C_y can each be determined by two separate calculations, and we perform both as validation (to within numerical error).

4.1. I) Circle in ellipse

The analytical solution for Stokes flow between concentric and offset circular cylinders demonstrates a dependence of the forces and torque experienced by the rod on the geometry of the domain (Finn & Cox 2001). We first consider how these results change when the bounding cylinder is elliptical. To limit the candidate geometries, we position the rod along the x -axis, i.e. $\mathbf{X} = (X, 0)$. We fix the cross-sectional area and set $R_o = 2$.

For a circular rod translating within a circular cylinder, K_{xx} and K_{yy} increase as the rod approaches the edge of the bounding cylinder (Slezkin 1955). For $e_o > 0$, the same behaviour occurs. We plot K_{xx} as a function of relative offset (which varies from 0 when the rod is concentric to 1 when the rod touches the boundary*) in Figure 8a for $e_o = 0$, $e_o = 0.6$, and $e_o = 0.8$ (lines *i*, *ii*, and *iii*, respectively). For each offset value, K_{xx} increases with e_o , though it should be noted that when plotting K_{xx} as a function of absolute offset X , a crossing of the curves is observed (see inset plot in Figure 8a); this is due to the fact that with higher eccentricity, there is a larger absolute distance to the edge. In all cases we compute the lift force $K_{xy} = 0$ (to within numerical error), which is expected by the symmetry of the domain.

*For all e_o values shown, the rod can fit tangent to the vertex, so $X/(a_o - 1) = 1$ is achievable.

We find that K_{yy} also increases monotonically as a function of offset (not plotted), though K_{yy} does exhibit an interesting dependence on e_o : in Figure 8b, we plot K_{yy} as a function of e_o for a centered rod, and we observe a non-monotonic behaviour. This reflects the complexity of boundary interactions: as the eccentricity increases, the proximity to the boundary in the vertical direction decreases while the distance to the boundary in the horizontal direction increases, and at nonequal rates.

We next consider the coupling coefficients C_x and C_y . For concentric circular cylinders, there is no coupling between translation and rotation, i.e., $C_x = C_y = 0$ (see Section 1.2). However, coupling does occur when there is an offset; e.g. when the rod is rotating and positioned away from the centre of the outer cylinder, the viscous fluid provides both an opposing torque and a force orthogonal to the minimal spacing. The force parallel to the minimal spacing in this scenario is zero (Slezkin 1955). We now explore how these results extend for a circular rod in an outer elliptical cylinder. We determine that, as with a circular outer cylinder, if the rod is offset in the x -direction, the coupling coefficient $C_x = 0$, while $C_y \neq 0$ for all e_o with $X \neq 0$. In Figure 8c we plot C_y as a function of relative offset for $e_o = 0$, $e_o = 0.6$, and $e_o = 0.8$ (lines *i*, *ii*, and *iii*, respectively). As observed by the crossing of the curves, for small relative offset the coupling is highest for the circular rod, while for large offset the most eccentric rod has the largest coupling coefficient. That is, as the inner rod approaches the edge of the domain, the fluid couples rotation to vertical force (and likewise vertical velocity to torque) more strongly for increased eccentricity. Again, the picture appears differently when plotted against absolute offset, since a greater total distance is available with increased eccentricity: for each absolute distance X , C_y decreases with eccentricity (plotted in the inset). As eccentricity increases, the domain approaches one of a circular rod between parallel plates. An asymptotic approximation to the Stokes force and torque on a cylinder rotating between parallel plates was obtained by Yang *et al.* (2013), where the ratio of gap width to cylinder radius defines the small parameter, ϵ . When the cylinder lies on the centreline between the two plates, $C_x = C_y = 0$; this may explain the behaviour of the lines in the inset of Figure 8, which approach zero as e_o increases (for moderate X values). We note that although the asymptotic solution Yang *et al.* (2013) is for a rotating cylinder, C_x and C_y still additionally characterise the torque generated via translational motion.

For a centred ($X = 0$) circular cylinder, the coefficient A_{zz} , which we recall characterises the resistance to rotation, increases with e_o , but is non-monotonically related to e_o when the cylinder is offset (results not shown). To further test whether the resistance coefficients for a rod in an elliptic cylinder approach those for a rotating rod between parallel plates (Yang *et al.* 2013), we consider a rod at $X = 0$ in an elliptic cylinder of fixed minor axis, $b_o = 1.025$, which fixes the gaps between the rod and the cylinder at $x = 0$, to be 0.025. In Figure 8d we then plot A_{zz} as a function of outer eccentricity (line *v*), and we see that as $e_o \rightarrow 1$ the resistance approaches the value for parallel plates with $\epsilon = 0.025$ (Yang *et al.* 2013). As we increase e_o with fixed minor axis, the cross-sectional area of the elliptic cylinder is also increasing. Thus, as a further geometric comparison, line *vi* plots A_{zz} for a rod centred in a circular cylinder with increasing and equivalent cross-sectional area (i.e. for each e_o , the bounding circle has cross-sectional area equal to that of an ellipse of eccentricity e_o and minor axis $b_o = 1.025$). Although A_{zz} decreases with e_o due to the increase in cross-sectional area available for the fluid, A_{zz} is larger when the outer boundary is an ellipse compared to a circle of the same cross-sectional area.

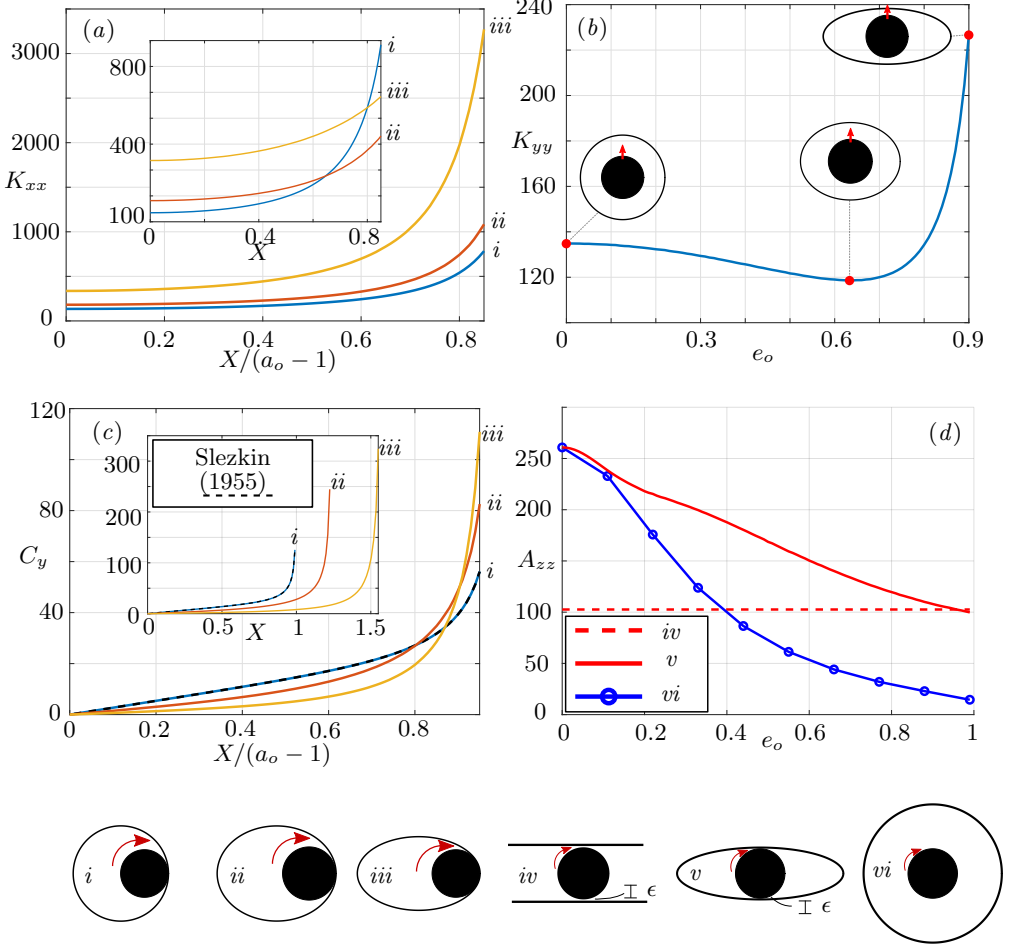


Figure 8: Results for $R_o = 2$. (a) Rod of unit radius centred at $(X, 0)$, translating with unit velocity in the x -direction. K_{xx} is plotted both as a function of relative offset and of X (inset) for three values of e_o : (i) $e_o = 0$ (ii) $e_o = 0.6$ and (iii) $e_o = 0.8$. (b) Rod translating with unit velocity in the y -direction, centred at $(0, 0)$. C_y is plotted as a function of e_o . Inset schematics are for (left-right) $e_o = 0$, $e_o = 0.63$, and $e_o = 0.9$. (c) Rod centred at $(X, 0)$, rotating with unit velocity in the clockwise direction for (i) $e_o = 0$, (ii) $e_o = 0.6$, and (iii) $e_o = 0.8$. The solution for $e_o = 0$ is compared against the analytical solution – Slezkin (1955), dashed black line. The main plot is function of relative offset, and inset is a function of X . (d) Plot of A_{zz} for a circular rotating rod centred at $(0, 0)$. The rod is rotating: (iv) between parallel plates with gap size $\epsilon = 0.025$ (Yang *et al.* 2013) (v) within an outer elliptic cylinder with $b_o = 1.025$ (R_o not fixed) (vi) within an outer circular cylinder of radius $R_o = 1.025(1 - e_o^2)^{-1/4}$. Solution obtained from equation (1.3c).

4.2. II) Ellipse in circle

The next domain we consider is an ellipse in a bounding circle. As in Section 3.2, due to the rotational symmetry of the outer domain, the number of unique combinations of position and orientation of the rod can be reduced; it is sufficient to consider the rod centred at $\mathbf{X} = (X, 0)$ and to vary X , Θ , and e_i . In Figure 9 we investigate how

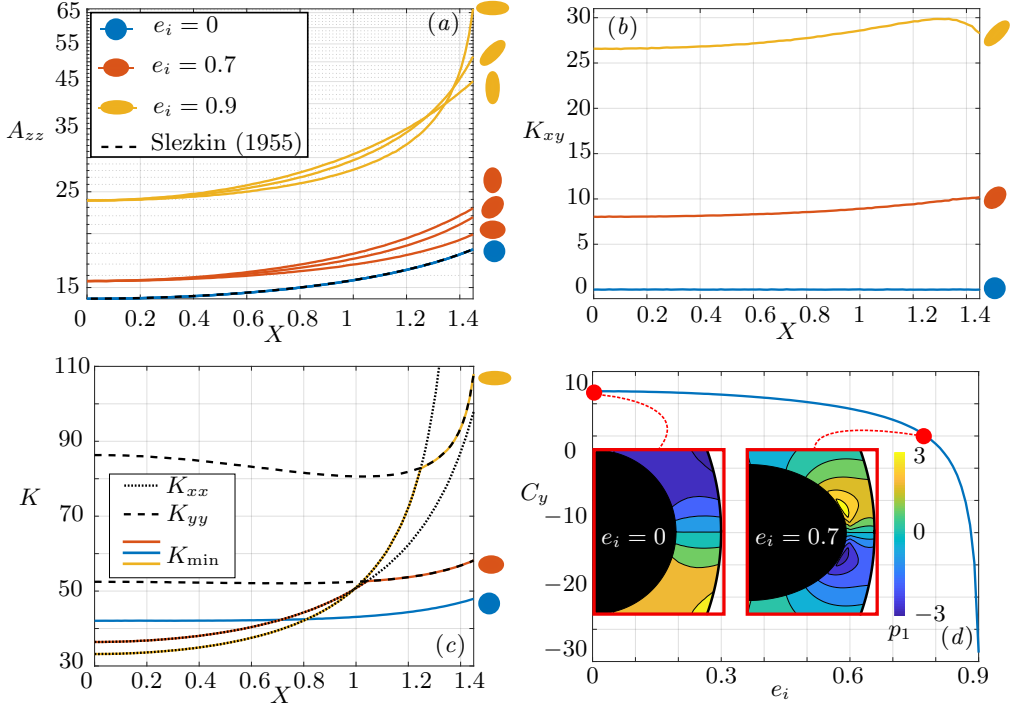


Figure 9: Figure (a) and (b) give A_{zz} and K_{xy} , respectively, as functions of X for $e_i = 0$, $e_i = 0.7$, and $e_i = 0.9$ and $\Theta = 0$, $\Theta_0 = \pi/4$, and $\Theta = \pi/2$. In (b), K_{xy} is identically zero for $\Theta = 0$ and $\Theta = \pi/2$, so these are not shown as they coincide with the line for $e_i = 0$. Figure (c) displays K_{\min} for $\Theta = 0$ and $e_i = 0$, $e_i = 0.7$, and $e_i = 0.9$. Figure (d) gives C_y as a function of e_i for $\Theta = 0$ and $X = 1.45$. Colormaps of pressure p_1 near the bounding wall, due to an imposed angular velocity, are shown for $e_i = 0$ and $e_i = 0.7$ with the colorbar providing the magnitude of p_1 , centred around $p_1 = 0$. All plots have a dimensionless outer radius of $R_o = 3$.

the resistance coefficients are influenced by the shape of the rod's cross-section and its orientation and proximity to the outer boundary. In Figure 9a-c, results are plotted as functions of absolute offset, and the orientation of the rod, Θ , as well as its position, X , determine the proximity of the boundary, and in a non-trivial way.

We first consider resistance to rotation. We find that A_{zz} increases as a function of offset for fixed e_i and Θ . Results are shown in Figure 9a for three eccentricities, $e_i = 0$, $e_i = 0.7$, and $e_i = 0.9$, oriented at $\Theta = 0$, $\Theta = \pi/4$, and $\Theta = \pi/2$. For fixed position and orientation, rotational resistance increases with eccentricity. Without boundary interactions, A_{zz} would be independent of Θ ; however due to the presence of the bounding circular cylinder, for moderate $X \neq 0$, A_{zz} is largest when $\Theta = \pi/2$ and smallest when $\Theta = 0$. As evidenced by the crossing lines for $e_i = 0.9$ in Figure 9a, when X is sufficiently large, a rod oriented at $\Theta = 0$ receives the largest opposing torque, which is likely due to the proximity of the vertex of the major axis to the boundary. We note that, if we increase the X range in Figure 9a, this effect is also seen for $e_i = 0.7$ [‡].

Turning now to translational resistance, our results validate the intuition that when the major or minor axis of the rod's cross-section is aligned both with the direction of

[‡]Results shown in Figure 16 (Appendix D)

motion and a radial line of the outer cylinder's cross-section, the force on the rod acts parallel to its direction of motion, and the lift force is zero. Brenner (1962a) proved this to be true for the motion of a bounded arbitrary particle.

Of the three translational resistances, we first consider the lift force, K_{xy} . We find, that for fixed e_i and X away from the boundary, K_{xy} is maximised for $\Theta = \pi/4$. Thus the outer cylinder does not seem to change classic results for an elliptic cylinder in an unbounded fluid (Lee & Leal 1986). To see how the lift force changes with inner eccentricity, in Figure 9b we fix the orientation at the maximal value $\Theta = \pi/4$ for eccentricities $e_i = 0$, $e_i = 0.7$, and $e_i = 0.9$, and plot K_{xy} as a function of X . We find a significant increase in lift force with eccentricity, and also a non-monotonic relation with position in the case of $e_i = 0.9$.

Next, we analyse K_{xx} , K_{yy} , and K_{\min} . For relatively small offset, K_{xx} is smallest (and K_{yy} largest) when $\Theta = 0$. We restrict to this orientation, and plot K_{xx} (dotted line) and K_{yy} (dashed line) as functions of X for $e_i = 0.7$ and $e_i = 0.9$ in Figure 9c. An interesting feature is the non-monotonic behaviour of K_{yy} with X . The solid coloured lines give the value of the minimum resistance, K_{\min} . Looking particularly at $e_i = 0.9$ we see that for small values of X , K_{\min} coincides with K_{xx} (and thus the eigenvector $\mathbf{k}_{\min} = \mathbf{e}_x$). However, near $X = 1.2$ the lines K_{xx} and K_{yy} cross, and the direction of minimum resistance switches to be aligned with the y -axis. The same behaviour is seen for $e_i = 0.7$, with the switching occurring at a smaller offset (near $X = 1$). The solid lines denoting K_{\min} for each eccentricity also cross. When X is small, K_{\min} is largest for $e_i = 0$ and smallest for $e_i = 0.9$ and vice versa for large X . Again, this can be explained by the significance of boundary interactions: far from the boundary the more eccentric ellipse has a direction of small resistance – its major axis – but closer to the boundary the major vertex is in closer proximity to the boundary, compared to ellipses of smaller eccentricity, hence the resistance in both the x - and y -directions rapidly increases. We have also demonstrated that for $\Theta = \pi/2$, \mathbf{k}_{\min} is aligned with the y -axis for $e_i = 0$, $e_i = 0.7$, and $e_i = 0.9$ (at least for $0 \leq X \leq 1.45$)‡.

Finally, we consider the coupling between translation and rotation. We find, for fixed e_i and X away from the boundary, C_x is largest for $\Theta = \pi/4$ and C_y is largest for $\Theta = \pi/2$ ‡. When the rod is oriented at $\Theta = 0$, there is coupling between rotation and translation in the y -direction ($C_y \neq 0$). This is known analytically for $e_i = 0$ (Slezkin 1955), and in this classic case, C_y increases monotonically with X . Interestingly, for more eccentric ellipses, this is no longer true; in fact, C_y can change sign as a function of position along the X -axis. Alternatively, this behaviour can be illustrated by plotting C_y as a function of eccentricity and fixed X sufficiently close to the outer boundary. This is shown in Figure 9 for $X = 1.45$ (the furthest-right position in Figures 9 (a)-(c)). We observe that C_y decreases as a function of e_i , changing sign from positive to negative. To explain this behaviour, consider a rotating rod with imposed angular velocity, in which case C_y characterises the induced translational force in the y -direction. Example pressure profiles for $e_i = 0$ and $e_i = 0.775$ near the proximal boundary are shown in the insets, and these show that the pressure drop in the lubrication layer between the rod and the outer boundary changes direction as a function of e_i . Due to the proximity to the boundary, we can appeal to Reynolds' lubrication equation to understand this inversion in terms of the behaviour of the fluid in the lubrication layer: for a circular surface *rotating* near a fixed plane, the pressure drop is in the opposite direction compared to the pressure drop for a highly curved surface *moving parallel* to the plane (Wannier 1950). For our system, rotating an ellipse of high eccentricity is analogous to moving the vertex (and point closest to the boundary) parallel to the boundary, whereas rotating an ellipse of

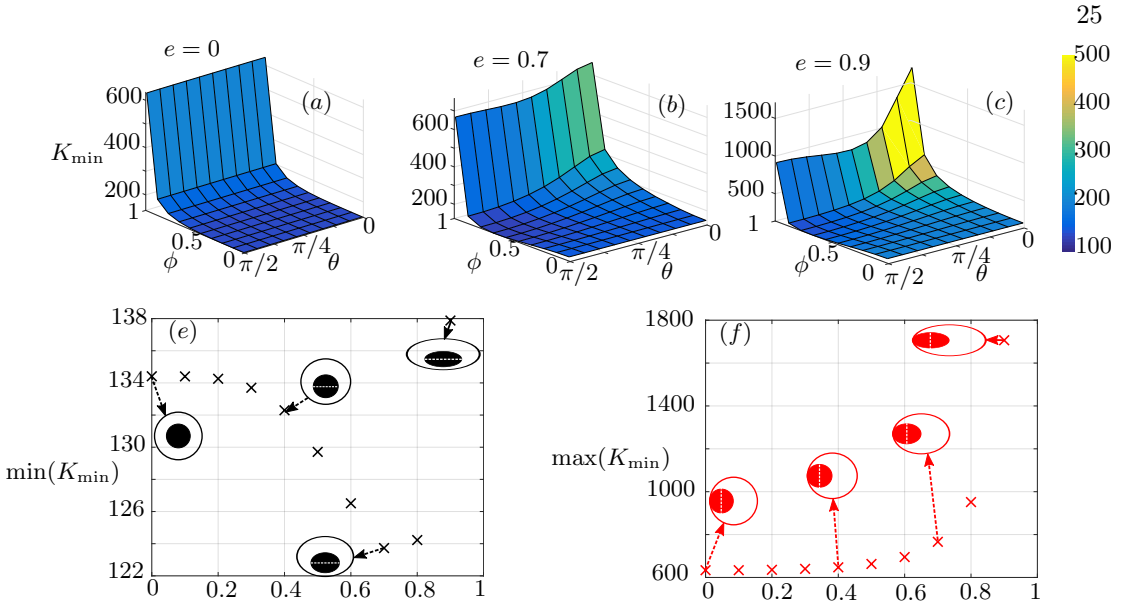


Figure 10: Surface plots (a)-(c) give the value of K_{\min} as a function of both offset, ϕ , and angular position θ (where these values are defined as in Section 3) of the inner ellipse for three different eccentricity values: (a) $e = 0$, (b) $e = 0.7$, and (c) $e = 0.9$.

Plots (d) and (e), respectively, show the maximum and minimum value of K_{\min} gives the minimum value of K_{\min} for a given equal inner and outer ellipse eccentricity value. The geometries that provide the $\min(K_{\min})$, (d), and $\max(K_{\min})$, (e), for $e = 0$, $e = 0.4$, $e = 0.7$, and $e = 0.9$ are demonstrated by diagrams and the white-dashed line on each of these shows the direction of minimum resistance. $R_o = 2$.

small eccentricity does not change significantly the minimal distance to the boundary and hence behaves more like a rotating circle.

4.3. III) Ellipse in ellipse

In this section we revisit the configuration considered in Section 3.3, with both the rod and bounding cylinder having elliptical cross-sections of the same eccentricity, e , and orientation ($\Theta = 0$). We set $R_o = 2$, and parameterise \mathbf{X} by offset ϕ and angular position θ , illustrated in Figure 5. Returning to Figure 6, the direction of minimum resistance is marked with a dashed white line. We see that when the rod is centred in the outer cylinder, \mathbf{k}_{\min} lies along the major axis of the ellipse. As we move towards the wall, this direction switches to the minor axis, due to the build-up of pressure between the rod and the proximal edge of the outer cylinder. As we break symmetry and vary θ , \mathbf{k}_{\min} no longer lies along an axis of symmetry of the inner ellipse and for $\phi = 0.99$ it varies from vertical for $\theta = 0$ to horizontal for $\theta = \pi/2$, see Figures 6 (e)-(g).

Figures 7a-c showed the axial flow rate in the (ϕ, θ) parameter space for three different eccentricity values, and in Figure 10a-c, we plot K_{\min} for the same domains. The minimum resistance is highest at the boundary, $\phi \rightarrow 1$, and at the orientation $\theta = 0$, and is generally larger in magnitude as eccentricity increases. The smallest value of K_{\min} represents the ‘most unstable’ position; for both $e = 0.7$ and $e = 0.9$ this occurs at $\theta = \pi/2$ and an intermediate ϕ value $0 < \phi < 1$. Here K_{\min} is in the x -direction, aligned with the major axis of the rod. This is similar to the behaviour determined by Dvinsky & Popel (1987) of a circular cylinder translating between two plates, parallel to the

boundaries, where the lowest force was incurred at a position between the centreline and the wall, with the exact location being dependent upon the ratio of the radius of the cylinder to the distance between the walls.

In Figure 10d, the minimum value of K_{\min} over (ϕ, θ) -space is plotted as a function of e . Several points have been illustrated to show the domain that produces the value, and the \mathbf{k}_{\min} axis is demonstrated on these by a dashed white line. We see that K_{\min} has a local minimum near $e = 0.7$. Note also that the position where the minimum K_{\min} is achieved changes with e , moving from the centre of the outer cylinder to the edge with increasing eccentricity. Figure 10e shows the maximum value of K_{\min} for increasing eccentricity, and again, the locations along with the \mathbf{k}_{\min} axis that produces these values is demonstrated at four points. Here there is a monotonic increase with eccentricity, and the location of the maximum K_{\min} always occurs on the major axis of the outer cylinder, closest to the wall ($\theta = 0, \phi = 0.99$).

Connecting these results with those in Section 3.3, we find the result that for each e , the location where K_{\min} is maximised coincides with the position where Q is maximised. Since a large value of K_{\min} corresponds to large resistance to the motion of the rod, we conclude that (at least in the case of cylinders of equal eccentricity and orientation) the configuration that provides maximum axial flow is also the most stable to cross-sectional motion.

5. Trajectories of the rod

In computing resistance coefficients, the rod is prescribed an ‘instantaneous’ motion from which we compute resulting forces and torque. The above result relating maximal flow to most stable position holds for cylinders of equal eccentricity and orientation. This suggests an intriguing dynamic for a rod that is free to change its cross-sectional position: *will the flow naturally push a rod to its most stable position and to where the flow is also optimal?* In this section we briefly explore this by solving the equations of motion (2.28) to determine trajectories of the rod. We begin by prescribing the initial position, orientation angle, translational velocity and angular velocity of the rod, equations (2.31). We then solve equations (2.24) and (2.34) subject to no-slip conditions (2.26a,b) and (2.27a) to calculate u , v , and p_1 . As in Section 4, we use these to compute \mathbf{F} and τ via equations (2.39). Using these, we update the velocity of the rod, using the relationships between linear and angular acceleration and force and torque, equations (2.28). We employ a numerical approximation of equations (2.28)

$$\dot{\mathbf{X}}^{i+1} = \alpha \mathbf{F}^i \Delta t + \dot{\mathbf{X}}^i, \quad \dot{\Theta}^{i+1} = \alpha' \tau^i \Delta t + \dot{\Theta}^i, \quad (5.1a,b)$$

where the superscripts denote the iteration number and Δt is the time-step. We then update the position and orientation of the rod using

$$\mathbf{X}^{i+1} = \dot{\mathbf{X}}^{i+1} \Delta t + \mathbf{X}^i, \quad \dot{\Theta}^{i+1} = \dot{\Theta}^i \Delta t + \Theta^i. \quad (5.2a,b)$$

We then repeat the calculation for updated position and velocities. Recall that in the parameter regime considered, fluid inertia is always negligible, hence the fluid is quasistatically updated during the rod motion. We present results for a domain of inner and outer ellipses of equal eccentricities 0.8, with $R_o = 2$, where the inner ellipse is given an initial unit translational velocity in the direction of \mathbf{k}_{\min} [‡]. In Figure 11 we compare

[‡]We take $\alpha = 10^{-2}$ to generate larger motion and easier visualization; while this technically violates our assumed balance $\alpha = O(1)$, the results presented below qualitatively hold for larger α .

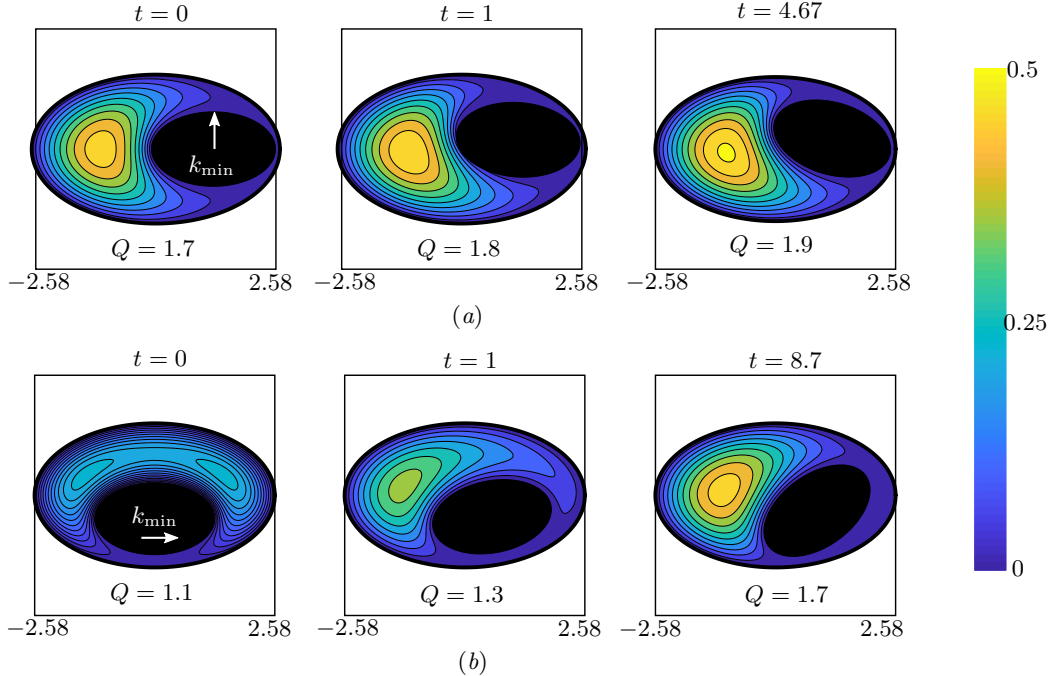


Figure 11: Three snapshots of the trajectory for rod subject to an initial unit velocity in the direction of \mathbf{k}_{\min} for $e = 0.8$ and $\Theta = 0$. The \mathbf{k}_{\min} direction is indicated by the white arrow. Here $\alpha = 10^{-2}$, $\alpha' = 4/(a_i^2 + b_i^2)^{-1}\alpha$, $\Delta t = 10^{-2}$. In (a) the initial position is where K_{\min} is minimised, and in (b) the initial position is where K_{\min} is maximised for the same domain.

the trajectories of a rod starting from its most stable (Figure 11 (a)) and least stable (Figure 11 (b)) positions, with initial velocity in the direction of least resistance, \mathbf{k}_{\min} , and with zero initial angular velocity. It is important to note that ‘least/most stable’ refers to our calculation in a restricted geometrical space, while in this motion there is no such restriction. In each case we show three snapshots of trajectories at times $t = 0$, $t = 1$, and $t = T_{\text{end}}$, where T_{end} is taken to be the time when \dot{X} , \dot{Y} , and $\dot{\Theta}$ are all less than some small value, δ , i.e., when the rod has reached an approximately stationary position. From the Stokes descriptions of the forces and torque experienced by the rod, we know they are always negative. Hence, the rod will always come to rest as $t \rightarrow \infty$.

In Figure 11a, we see that the inner ellipse initially moves upwards, in the direction of the applied velocity, before rotating, due to torques generated as a result of interactions with the boundary. It reaches the stationary criteria at time $T_{\text{end}} = 4.67$, such that the linear distance between the initial position of the ellipse centre and its final position is 0.2272. In Figure 11b, we see similar behaviour, however the rod takes longer to come to rest ($T_{\text{end}} = 8.7$), and its final position is a distance 0.9086 from its initial position. Thus, the elliptical cylinder starting in the ‘least stable’ location of minimum K_{\min} (Figure 11 b) moved four times as far as the one starting in the ‘most stable’ location of maximum K_{\min} (Figure 11 a). In Figure 11, we have also plotted the axial velocity profiles for each domain with the corresponding flux values. It is interesting to observe that in both simulations, as the position of the inner ellipse evolves, the axial volumetric flow rate increases.

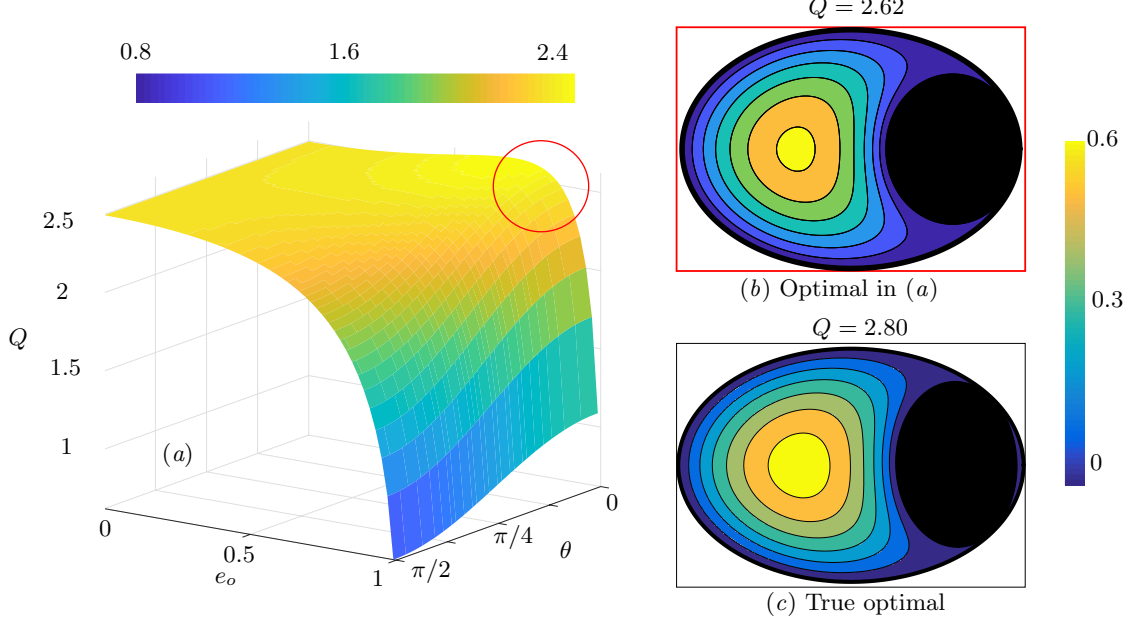


Figure 12: A plot of Q as a function of e_o and θ for $R_o = 2$. Here the inner ellipse touches the outer boundary tangentially at a single point, matching curvature. The red circle indicates the presence of a global maximum.

6. Optimal geometry for axial flow

When considering the ellipse in ellipse geometries in Sections 3 and 4, we constrained the shapes of the inner and outer ellipses to have the same eccentricity, $e = e_o = e_i$, and orientation, $\Theta = 0$. We found in 3.3 an eccentricity value and position for the inner ellipse that maximised Q within this parameter space. However, this is not necessarily the configuration that will maximise flux over the full parameter space, (e_o, e_i, X, Y, Θ) , and in this section we explore finding a global optimal geometry for fixed cross-sectional area, $R_o = 2$. For all configurations previously considered, we demonstrated that axial flow resistance was lowered by increasing the distance between the centres of the inner and outer ellipses. Intuitively, we might expect that the optimal configuration is one where the inner ellipse touches the boundary of the outer ellipse and with matching curvature, i.e. when the inner ellipse ‘hugs’ the outer. This assumption enables a reduced parameter space that can be approached analytically (see Appendix E). In Figure 12a we show a surface plot of Q as a function of e_o and θ produced by this calculation. We see that a global maximum occurs at $\theta = 0$ and $e_o \approx 0.71$ with corresponding $Q = 2.62$ (indicated by the red circle and corresponding flow profile Figure 12b). (At this maximum, we also have $e_i \approx 0.45$, $\Theta = 0$.)

The optimal configuration in Figure 12a shows a nearly 40% improvement in flux over the optimal configuration computed in Section 3.3. However, it is still not sufficient to claim this as the global optimum for ellipse geometries. In fact, a parameter sweep over e_i , X , Y , and Θ , for fixed e_o , indicates that a ‘curve-hugging’ configuration may not be optimal (Appendix F). Motivated by this, we relax assumptions about how the ellipses meet at the boundary and formulate an optimisation problem to traverse the full parameter space. To this end, we define a vector, \mathbf{g} , containing the five parameters

governing the geometry of the domain

$$\mathbf{g} = (e_i, e_o, X, Y, \Theta)^T. \quad (6.1)$$

The boundaries of the inner and outer ellipses, Γ_i and Γ_o , are

$$\mathbf{x}^T \mathbf{A} \mathbf{x} = 0, \quad \mathbf{x}^T \mathbf{B} \mathbf{x} = 0, \quad (6.2a,b)$$

respectively, where $\mathbf{x}^T = (x, y, 1)$ and matrices \mathbf{A} and \mathbf{B} are functions of \mathbf{g} . Thus, we seek the solution to the optimisation problem

$$\min_{\mathbf{g}} -Q, \quad \text{s.t. } \mathbf{c} \geq 0, \quad (6.3)$$

where \mathbf{c} is a vector of six non-linear constraints, dependent on \mathbf{A} and \mathbf{B} and hence \mathbf{g} , that ensure Γ_i is enclosed by Γ_o (see Appendix G for more details). We solve equation (2.35) in FEniCS (Alnaes *et al.* 2015), and implement MATLAB's optimisation routine, `fmincon`, to solve the optimisation problem (6.3) with an interior-point method from eight randomly generated starting points in the feasible five-dimensional parameter space. As the optimisation routine seeks local minima, a multi-start approach allows for global optimisation. The optimal geometry found through this method is shown in Figure 12c with a corresponding flux, $Q \approx 2.80$. The geometric parameters (see equation 6.1) are $\mathbf{g} \approx (0.68, 0.74, 1.49, 0, \pi/2)^T$. This global optimum gives a non-negligible (nearly 7%) increase in flux compared with the 'curve hugging' optimum. Indeed, rather than perfectly matching the geometries at the boundary, the global optimal geometry is tangent to the outer boundary in two locations (this was also true in the results in Section 3.1.) It is interesting to note that this divides the fluid domain into two separate regions, which may be connected to previous results (Ranger 1994, 1996) that demonstrated flux enhancement through creating multiply connected regions.

7. Discussion

We have considered in this paper the effect of geometry in an annular region, formed by an elliptic rod and coaxial elliptic cylinder, on two types of resistance: the resistance to axial flow, and the resistance to movement of the rod in the cross-section. This research was motivated by questions of optimal device design: where to position the rod, and how to shape the cross-sections of the rod and the bounding cylinder, to maximise axial flux and minimise movement of the rod? Motivated by the design of urological devices, we have restricted to the parameter regime in which the fluid behaviour is dominated by viscous forces, but in which inertia of the inner cylinder is non-negligible. In this regime, we showed that the axial flow decouples from the cross-sectional flows. Therefore, we can separately solve a Poiseuille flow problem for the axial flow and Stokes flow in the cross-section, with the profile of the cross-sectional flow producing a net force and torque that couple to the motion of the inner cylinder.

7.1. Axial flow resistance

For all configurations considered, the flux increases monotonically as the rod is positioned further from the centre of the outer cylinder, and the maximum flux is achieved when the rod touches the boundary of the outer cylinder. For a circular rod in a circular cylinder, the maximum flux is achieved when the circle touches the outer boundary at a single point (Snyder & Goldstein 1965; MacDonald 1982). When either the outer cylinder or the rod is elliptical, we found that flow can be increased from the circular case by touching the boundary tangentially at two points. Even within the reduced space

of elliptical cylinders, the full optimisation problem is 5-dimensional and non-trivial, containing many local minima. Along with the global optimum, we have also considered several constrained optimisation problems; these are summarised in Table 3, grouped by geometric constraint. Of particular relevance is the fact that the global optimum gives a 52% increase over the circle in circle case. Also of note is the observation that the true optimum in the case of an ellipse in circle, circle in ellipse, and ellipse in ellipse, all occur at configurations for which the inner cylinder meets the outer cylinder at two tangent points and thus does not correspond to a matching of the curvature of the boundaries.

7.2. Cross-sectional flow resistance

The cross-sectional resistance to imposed translational and rotational movement of the rod is fully characterised by six unique scalars. The behaviour of these resistance coefficients is determined both by the shape of the rod's cross-section and its proximity to the bounding cylinder. When varying eccentricity, position, and orientation, and the impact on 6 scalars, we are thus faced with a very high-dimensional parameter space to investigate. Our results do not represent a complete sweeping of all configurations; rather we have tried to uncover trends, to compare with classic results in particular limits, and to focus on unexpected behaviour. One particularly interesting result was found for an elliptic rod near the edge of a bounding circular cylinder, in which case we found that the sign of the coefficient coupling translational and rotational motion changed as the eccentricity of the inner ellipse increased. This result could be rephrased as a change in motion being generated by a change in shape, and we might speculate whether such a process could be harnessed in a micro-swimming context, where trajectories are determined by principles of Stokes resistance (Lauga & Powers 2009).

It is important to note that all resistance coefficients diverge as the rod approaches the outer boundary. Thus, positions for the rod which lead to high axial flux (close to the edge of the bounding cylinder) receive extremely high resistance to translational and rotational motions. We defined the ‘most stable’ configuration as the one where the minimum translational resistance is maximum; i.e. for which the fluid provides the strongest resistance to translational motion in the direction that is easiest to move. Thus, it is impossible to fully connect configurations of maximum axial flux to positions of highest minimal resistance within our modelling framework, as the maximum axial flow occurs when the rod touches the wall, and here the resistance always diverges. Nevertheless, for the particular class of an elliptic rod in an elliptic cylinder of the same eccentricity and orientation, we restricted the parameter space of rod positions to those not touching the boundary, and found that the geometry that maximises axial flux is also the most stable.

7.3. Trajectories

Motivated by the coinciding of configurations for optimal axial flow and maximal stability, we also considered rod trajectories by integrating forward the equations of motion for the inner rod. Here we must be careful not to disconnect the results from the parameter regime: rod inertia was included in our calculations while fluid inertia was neglected. In this regime we could quasi-statically update the forces and torques on the rod after updating its position and resolving the Stokes equations in the cross-section.

In the two cases considered (Figure 11), we observed an increasing axial flux throughout the motion, as well as a negative correlation between stability of the initial position and magnitude of motion (quantified via distance from initial position). While more work is needed to fully understand how a rod will move in these geometries, we obtain at least

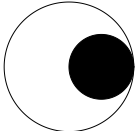
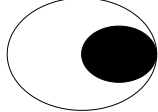
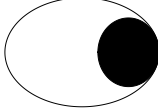
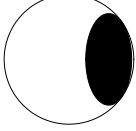
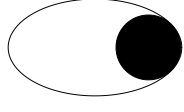
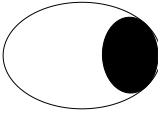
Description	Optimal Configuration	Geometry	Q	Tangent points
Circle in circle		$e_i = 0 \quad e_o = 0$ $X = 1 \quad Y = 0$ $\Theta = 0$	1.84	1
Ellipse in ellipse ($e_i = e_0$, $\Theta = 0$)		$e_i = 0.66 \quad e_o = 0.66$ $X = 1.15 \quad Y = 0$ $\Theta = 0$	1.89	1
Ellipse in ellipse (‘curve hugging’)		$e_i = 0.45 \quad e_o = 0.71$ $X = 1.44 \quad Y = 0$ $\Theta = \pi/2$	2.62	1
Ellipse in circle		$e_o = 0 \quad e_i = 0.87$ $X = 1.23 \quad Y = 0$ $\Theta = \pi/2$	2.66	2
Circle in ellipse		$e_i = 0 \quad e_o = 0.83$ $X = 1.65 \quad Y = 0$ $\Theta = 0$	2.69	2
Ellipse in ellipse		$e_i = 0.68 \quad e_o = 0.74$ $X = 1.49 \quad Y = 0$ $\Theta = \pi/2$	2.80	2

Table 3: Summary of optimal configurations for $R_o = 2$.

an answer to the question of whether the rod will always naturally move to a position of maximum stability and optimal axial flow. The fact that the resting positions of the rods is not the global optimum (which would be against the wall), the answer is *no*. This is not surprising, actually, when one considers that the fluid is not really pushing the rod at all but merely dissipating energy that has to be input to the rod from the external

world. Of course, this would cease to be the case if the axial flow were coupled to the cross-sectional flow, which would be true if one breaks the co-axial assumption. It would be interesting to consider how such effects, as well as including fluid inertia, impact on our findings.

7.4. Conclusion

Low-Reynolds number flow in annular regions bounded internally and externally by ellipses is a surprisingly rich area of research. There are many industrial flows through cylinders containing a coaxial rod, such as oil wells and small-scale medical devices, and in these applications, it is often important to maximise the flux. Our results indicate that an understanding of the complex effect of geometry on resistance in annular domains can enhance optimal device design. Our work has particular impact in the field of endourology, where an understanding of the axial flow resistance and stable geometric configurations can help guide the design of surgical tools.

This publication is based on work supported (or partially supported) by the EP-SRC Centre For Doctoral Training in Industrially Focused Mathematical Modelling (EP/L015803/1) in collaboration with Boston Scientific. S.L.W. is grateful for funding in the form of a Royal Society Leverhulme Trust Senior Research Fellowship. The authors would like to acknowledge the support of Boston Scientific Corporation; in particular, helpful conversations were had with Niraj Rauniyar, Timothy Harrah, and Aditi Ray on the application of this work to ureteroscopy device design. The authors are also grateful for input from Matthias Heil on using **oomph-lib** (Heil & Hazel 2006).

REFERENCES

- ALNAES, M.S., BLECHTA, J., HAKE, J., JOHANSSON, A., KEHLET, B., LOGG, A., RICHARDSON, C., RING, J., ROGNES, M.E. & WELLS, G.N. 2015 The FEniCS Project Version 1.5. *Archive of Numerical Software* **3** (100), 9–23.
- BERGMAN, HARRY, ed. 1981 *The Ureter*, 2nd edn. Springer-Verlag.
- BRENNER, H. 1962a Effect of finite boundaries on the Stokes resistance of an arbitrary particle. *J. Fluid. Mech.* **12** (1), 35–48.
- BRENNER, H. 1962b Effect of finite boundaries on the Stokes resistance of an arbitrary particle, part 2. asymmetrical orientations. *J. Fluid. Mech.* **12** (1), 35–48.
- BRENNER, H. 1962c The Stokes resistance of an arbitrary particle. *Chem. Eng. Sci.* **18**, 1–25.
- BRENNER, H. 1963 The Stokes resistance of an arbitrary particle II (an extension). *Chem. Eng. Sci.* **19** (10), 599–629.
- BTAIT, U. G., GIBSON, G. M., HO, Y.-L. D., TAVERNE, M., TAYLOR, J. M. & PHILLIPS, D. B. 2019 Indirect optical trapping using light driven micro-rotors for reconfigurable hydrodynamic manipulation. *Nat. Commun.* **10** (1), 1215.
- CASEY, J. 1893 A treatise on the analytical geometry of the point, line, circle, and conic sections.
- CHWANG, ALLEN T. & WU, T. Y.-T. 1975 Hydromechanics of low-Reynolds-number flow. Part 2. Singularity method for Stokes flows. *J. Fluid Mech.* **67**.
- COX, S. M. & FINN, M. D. 2007 Two-dimensional Stokes flow driven by elliptical paddles. *Phys. Fluids* **19**.
- DVINSKY, A.S. & POPEL, A.S. 1987 Motion of a rigid cylinder between parallel plate in stokes flow - Part I: Motion in a quiescent fluid and sedimentation. *Comput. Fluids* **15** (4), 391–404.
- EBRAHIM, N. H., EL-KHATIB, N. & AWANG, M. 2013 Numerical Solution of Power-law Fluid Flow through Eccentric Annular Geometry. *AJNA* **1**.
- ETAYO, F. & GONZALEZ-VEGA, L. 2006 A new approach to characterizing the relative position of two ellipses depending on one parameter. *Comput. Aided Geom. Des.* **23**, 324–350.

- FINN, M. D. & COX, S. M. 2001 Stokes flow in a mixer with changing geometry. *J. Eng. Math.* **41**, 75–99.
- FRAZER, R.A. 1926 On the motion of cylinder in a viscous fluid. *Philos. Trans. Royal Soc. A*.
- HACKBORN, W.W. 1991 Separation in a two-dimensional Stokes flow inside an elliptic cylinder. *J. Eng. Math.* **25**, 13–22.
- HEIL, M & HAZEL, A 2006 Oomph-lib: an object-oriented multi-physics finite-element library. In *Fluid-Structure Interaction* (ed. M. Schäfer & H.-J. Bungartz), pp. 19–49. Springer.
- HEYDA, J. F. 1959 A green's function solution for the case of laminar incompressible flow between non-concentric circular cylinders. *J. Franklin Inst.* **267** (1), 25–34.
- HINCH, E. J. 1972 Notes on the symmetries of certain material tensors for a particle in Stokes flow. *J. Fluid Mech.* pp. 423–425.
- ISHIKAWA, T., SIMMONDS, M. P. & PEDLEY, T. J. 2006 Hydrodynamic interaction of two swimming model micro-organisms. *J. Fluid Mech.* **568**, 119–160.
- JEFFREY, D. J. & ONISHI, Y. 1981 The slow motion of a cylinder next to a plane wall. *Q. J. Mech. Appl. Math.* **34**, 129–137.
- JEFFREY, G.B. 1922 The rotation of two circular cylinders in a viscous fluid. *Philos. Trans. Royal Soc. A*.
- LAMB, H. 1916 *Hydrodynamics*. Fetter Lane, E.C.: Cambridge University Press.
- LAUGA, E. & POWERS, T.R. 2009 The hydrodynamics of swimming microorganisms. *Rep. Prog. Phys.* **72**, arXiv: 0812.2887.
- LEE, S.H. & LEAL, L.G. 1986 Low-Reynolds-number flow past cylindrical bodies of arbitrary cross-sectional shape. *J. Fluid Mech.* **164**, 401–427.
- MACDONALD, D. A. 1982 Fully developed incompressible flow between non-coaxial circular cylinders. *ZAMP* **33** (6), 737–751.
- ORATIS, ALEXANDROS T., SUBASIC, JOHN J., HERNANDEZ, NATALIA, BIRD, JAMES C. & EISNER, BRIAN H. 2018 A simple fluid dynamic model of renal pelvis pressures during ureteroscopic kidney stone treatment. *PLoS ONE* **13** (11).
- RANGER, K. B. 1994 Research note on the steady Poiseuille flow through pipes with multiple connected cross sections. *Phys. Fluids* **6**, 2224–2226.
- RANGER, K. B. 1996 Volumetric flux rate enhancement and reduction in conical viscous flows with multiply connected cross sections. *Chem. Eng. Comm.* pp. 143–160.
- REDBERGER, P.J. 1962 Axial laminar flow in a circular pipe containing a cixed eccentric core. *Can. J. Chem. Eng.* .
- SAATDJIAN, E., MIDOUX, N. & ANDRÉ, JC. 1994 On the solution of Stokes' equations between confocal ellipses. *Phys. Fluids* **6**, 3833–3846.
- SASTRY, U.A. 1964 Viscous flow through tubes of doubly connected regions. *Indian J. Pure Appl. Phys.* **3**, 230–232.
- SHIVAKUMAR, P.N. 1973 Viscous flow in pipes whose cross- sections are doubly connected regions. *Appl. Sci. Res.* **27**.
- SHIVAKUMAR, P.N. & CHUANXIANG, J. 1993 On the Poisson's equation for doubly connected regions. *CAMQ* **1** (4), 555–567.
- SLEZKIN, N.A. 1955 *Dynamics of a viscous incompressible fluid*. Moscow.
- SNYDER, W. T. & GOLDSTEIN, G. A. 1965 An analysis of fully developed laminar flow in an eccentric annulus. *A.I.Ch.E.* pp. 462–467.
- WANNIER, G.H. 1950 A contribution to the hydrodynamics of lubrication. *Q. Appl. Math.* **8**.
- WILLIAMS, J.G., TURNER, B.W., RAUNIYAR, N.P., HARRAH, T.P., WATERS, S.L. & MOULTON, D.E. 2019 The fluid mechanics of ureteroscope irrigation. *J. Endourol.* **33** (1), 28–34.
- WILSON, W. T. & PREMINGER, G. M. 1990 Intrarenal pressures generated during flexible deflectable ureterorenoscopy. *J. Endourol.* **4** (2), 135–141.
- YANG, J., WOLGEMUTH, C. W. & HUBER, G. 2013 Force and torque on a cylinder rotating in a narrow gap at low Reynolds number: scaling and lubrication analyses. *Phys. Fluids* **25**.

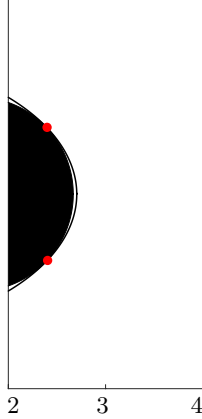


Figure 13: The geometry that maximises flux in Figure 3. A close-up of configuration (ii).

Appendix A. Position that maximises flux (Section 3.1)

The rod position that maximises axial flux for a circular rod in an elliptic cylinder is the position as close to the vertex of the bounding cylinder as geometrically possible. This will be when the radius of the inner circle is less than the radius of curvature of the ellipse at the vertex, which for a cylinder of major axis a and minor axis b is b^2/a .

Thus, for a circle of radius r , if $b^2/a \geq r$ then the rod position that maximises flux is $a - r$ from the centre of the ellipse. If $b^2/a < r$, we can solve for the position of the circle centre where the circle and the ellipse are tangent in two locations. This is $\sqrt{a^2 - b^2} \sqrt{1 - r/b^2}$ from the centre of the bounding ellipse.

Thus, for our configuration, the rod position that maximises flux is

$$X = a_o - 1, \text{ if } e_o \geq e^*, \quad X = a_o e_o \sqrt{1 - b_o^{-2}}, \text{ if } e_o < e^*, \quad (\text{A } 1a,b)$$

where

$$e^* = \sqrt{1 - R_o^{-4/3}}. \quad (\text{A } 2)$$

A closer look at the ellipse vertex for configuration (ii) in Figure 3 (the configuration that maximises flux over all e_o for $R_o = 2$) is shown in Figure 13. The two points of intersection between the rod and bounding cylinder are indicated by red dots. As the circle touches the ellipse in two locations, rather than just the vertex, the eccentricity of the ellipse is greater than e^* .

Appendix B. Domain transformation (Section 3.3)

Here we describe the coordinate transformation used in Section 3.1; we map a domain of an ellipse in an ellipse of equal eccentricities and orientations to a rectangle (this facilitates use of a finite-difference scheme). The centre of the inner ellipse cross-section in the (x, y) plane, $\mathbf{X} = (X, Y)$, is a distance d away from the centre of the outer ellipse, $(0, 0)$ at an angle θ from the x -axis as shown in Figure 14 (i) so that

$$\mathbf{X} = (d \cos(\theta + \pi), d \sin(\theta + \pi)). \quad (\text{B } 1)$$

We first shift the centres of the circles along the x -axis by q_o , which we define in Section B.2. This is to allow for the subsequent usage of bipolar coordinates. The equations for

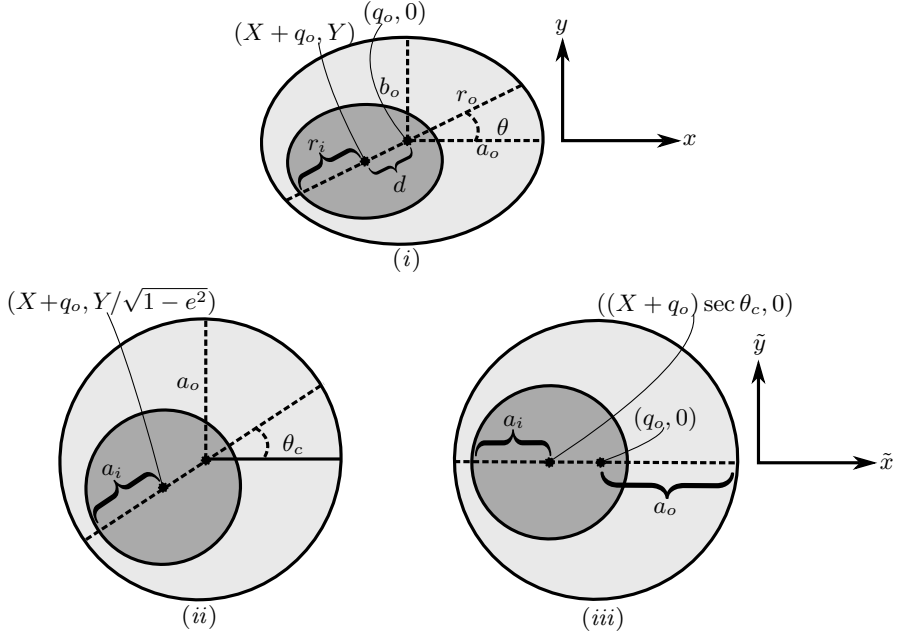


Figure 14: A two-step coordinate transformation maps the offset ellipses in Figure (i) to the offset circles in Figure (iii) whose centres both lie along the \tilde{x} -axis. In Figure (i) the ellipses both have eccentricity e with major axes a_i , a_o and minor axes b_i , b_o . The centre of the inner ellipse is offset from the x -axis by an angle θ and the radii of the inner and outer ellipses along a line connecting their centres are r_i and r_o , respectively. The coordinates of the centres of the inner and outer ellipse in the (x, y) coordinate system are $(X + q_o, Y)$ and $(q_o, 0)$, respectively. Figure (ii) depicts the domain after scaling the y -axis by $1/\sqrt{1 - e^2}$ to convert the ellipses to circles. Figure (iii) shows the domain after rotating the coordinates in (ii) so both centres now lie on the same axis in (\tilde{x}, \tilde{y}) coordinates.

boundaries of the curved surfaces Γ_i and Γ_o are then given by

$$(x - X - q_o)^2/a_i^2 + (y - Y)^2/b_i^2 = 1, \quad (x - q_o)^2/a_o^2 + y^2/b_o^2 = 1, \quad (\text{B2})$$

respectively. We transform the elliptical geometry in Figure 14 (i) to offset circles via the following steps.

B.1. Ellipses to circles

We scale the axes to transform the ellipses to circles, see Figure 14 (ii), and then rotate this new coordinate system so that the centre of the rod cross-section is located along the horizontal-axis of the new coordinate system, denoted \tilde{x} , see Figure 14 (iii). We introduce the change of variables

$$\tilde{x} = x \cos \theta_c - (\sin \theta_c / \sqrt{1 - e^2}) y - q_o \cos \theta_c + q_o, \quad (\text{B3a,b})$$

$$\tilde{y} = (x - q_o) \sin \theta_c + (\cos \theta_c / \sqrt{1 - e^2}) y - \sin \theta_c, \quad (\text{B3a,b})$$

from (x, y) to (\tilde{x}, \tilde{y}) . The scaling of the y -axis to transform the ellipses to circles appears as the $1/\sqrt{1 - e^2}$ factor in equation (B3). The angle θ_c , illustrated in Figure 14 (ii), is

given by

$$\theta_c = \arctan \left(Y \sqrt{1 - e^2} / X \right). \quad (\text{B } 4)$$

In terms of (\tilde{x}, \tilde{y}) the expressions for the inner and outer ellipses, equation (B 2), are now

$$(\tilde{x} - (X + q_o) \sec \theta_c)^2 + \tilde{y}^2 = a_i^2, \quad \tilde{x}^2 + \tilde{y}^2 = a_o^2, \quad (\text{B } 5)$$

respectively, which correspond to circles of radii a_i and a_o centred along the \tilde{x} -axis, see Figure 14 (iii). We find that

$$\phi = d/d_{max} = X \sec \theta_c / (a_o - a_i), \quad (\text{B } 6)$$

so ϕ is conserved through the coordinate transformation and the relative shift in the elliptical domain in Figure 14 (i) is the same as the relative shift in the circular domain in Figure 14 (iii).

B.2. Bipolar coordinates

To convert the offset circles to a rectangular domain we use a bipolar coordinate system defined by

$$\eta = \arctan [2c\tilde{x}/(\tilde{y}^2 + \tilde{x}^2 + c^2)], \quad \xi = \arctan [2c\tilde{y}/(\tilde{y}^2 + \tilde{x}^2 - c^2)], \quad (\text{B } 7a,b)$$

where lines of constant η correspond to non-intersecting, non-concentric circles of different radii centred along the x -axis. Constant parameter c is given by

$$c = a_i |\sinh \eta_i| = a_o |\sinh \eta_o|, \quad (\text{B } 8)$$

where η_i and η_o are constant η values parameterising circles of radii r_i and r_o with centres a distance d apart. These are given by

$$\eta_i = \cosh^{-1} [(\gamma(1 + \phi^2) + (1 - \phi^2))/(2\phi\gamma)], \quad \eta_o = \cosh^{-1} [(\gamma(1 - \phi^2) + (1 + \phi^2))/(2\phi)], \quad (\text{B } 9)$$

where $\gamma = a_i/a_o$. We note from equations (B 9) that η_i and η_o are defined and distinct for $0 < \phi < 1$. The outer circle is centred at x -value

$$q_o = c \coth \eta_o. \quad (\text{B } 10)$$

Equation (B 10) provides the initial shift along the x -axis in the domain. Thus, we have the required information to perform the coordinate transformation specified by equation (B 3) and to subsequently convert to Bipolar coordinates via equation (B 7). Under the transformations stipulated by equations (B 3) and (B 7), the governing flow equation (2.35) becomes

$$\alpha \frac{\partial^2 w_0}{\partial \eta^2} + 2\beta \frac{\partial^2 w_0}{\partial \eta \partial \xi} + \gamma \frac{\partial^2 w_0}{\partial \xi^2} + \Delta_1 \frac{\partial w_0}{\partial \eta} + \Delta_2 \frac{\partial w_0}{\partial \xi} = c^2, \quad (\text{B } 11)$$

where α , β , γ , Δ_1 , and Δ_2 , are functions of η and ξ given by

$$\left. \begin{aligned} \alpha(\eta, \xi) &= (\cos \xi \cosh \eta - 1)^2 (\cos^2 \theta + k^2 \sin^2 \theta) + \sin^2 \xi (k^2 \cos^2 \theta + \sin^2 \theta) \sinh^2 \eta, \\ \beta(\eta, \xi) &= (k^2 - 1) \cos(2\theta) (\cos \xi \cosh \eta - 1) \sin \xi \sinh \eta, \\ \gamma(\eta, \xi) &= (\cos \xi \cosh \eta - 1)^2 (k^2 \cos^2 \theta + \sin^2 \theta) + \sin^2 \xi (\cos^2 \theta + k^2 \sin^2 \theta) \sinh^2 \eta, \\ \Delta_1(\eta, \xi) &= (k^2 - 1) \cos^2 \theta (\cos \xi - \cos(2\xi) \cosh \eta) \sinh \eta, \\ \Delta_2(\eta, \xi) &= (k^2 - 1) \cos^2 \theta \sin \xi (\cos \xi \cosh^2 \eta + \cos \xi \sinh^2 \eta - \cosh \eta), \end{aligned} \right\} \quad (\text{B } 12)$$

for η_i and η_o given by equation (B 9). The no-slip boundary conditions, equations (2.36), are

$$f(\eta, \xi) = 0 \text{ on } \eta = \eta_i, \eta_o. \quad (\text{B } 13)$$

Additionally, we implement periodic boundary conditions in ξ , given by

$$f(\eta, 0) = f(\eta, 2\pi), \quad f\xi(\eta, 0) = f\xi(\eta, 2\pi). \quad (\text{B } 14)$$

We solve equation (B 11) with boundary conditions (B 13) and (B 14) with a finite difference scheme implemented in **Matlab**, using central differences to approximate the derivatives in equation (B 11) and one-sided differences to approximate the periodic boundary conditions in equation (B 14). We validated our numerics by comparing the results for circular domains to the analytical solution given by Snyder & Goldstein (1965) and for the elliptical domains we also solved equation (2.23) using finite elements in **oomph-lib** (Heil & Hazel 2006), demonstrating good agreement. Finally, we can use the computed velocity profiles to calculate the dimensionless volumetric flow rate, given by

$$Q = \int_0^{2\pi} \int_{\eta_o}^{\eta_i} \left| \frac{\partial(x, y)}{\partial(\eta, \xi)} \right| f d\eta d\xi, \quad (\text{B } 15)$$

which, after explicitly calculating the Jacobian of the transformation, becomes

$$Q = c^2 \sqrt{1 - e^2} \int_0^{2\pi} \int_{\eta_o}^{\eta_i} \frac{f}{(\cos \xi - \cosh \eta)^2} d\eta d\xi. \quad (\text{B } 16)$$

We approximate this integral numerically in **Matlab** with the trapezoidal rule.

Appendix C. Additional results (Section 3.3)

To complement the results in Section 3.3, we fix two of our three parameters (e , ϕ , and θ) and plot Q as a function of the third. Figure 15a shows a monotonic increase of Q with ϕ for $\theta = 0$ and $e = 0, 0.4, 0.65$, and 0.8 . Figure 15b captures a zoomed-in view of Figure 15a between $0.9 \leq \phi \leq 0.99$, and shows that over this range of ϕ , for the four eccentricity values plotted, $e = 0.65$ has the highest flux and $e = 0$ has the lowest. Figure 15c plots the non-monotonic relationship between θ and Q indicated by Figures 6e-h for $e = 0, 0.4, 0.65$, and 0.8 . The flux is largest for $\theta = 0$ and has a minimum between $\theta = \pi/4$ and $\theta = \pi/2$. For $e = 0$, Q is constant with respect to ϕ as expected due to the rotational symmetry of the domain. Figure 15 shows Q as a function of e for fixed offset, $\phi = 0.99$, and $\theta = 0, \pi/4$, and $\pi/2$. For $\theta = 0$, the flux is maximum for e between 0.6 and 0.8 . For $\theta = \pi/4$, there is a maximum Q near $e = 0.3$, whereas for $\pi/2$,

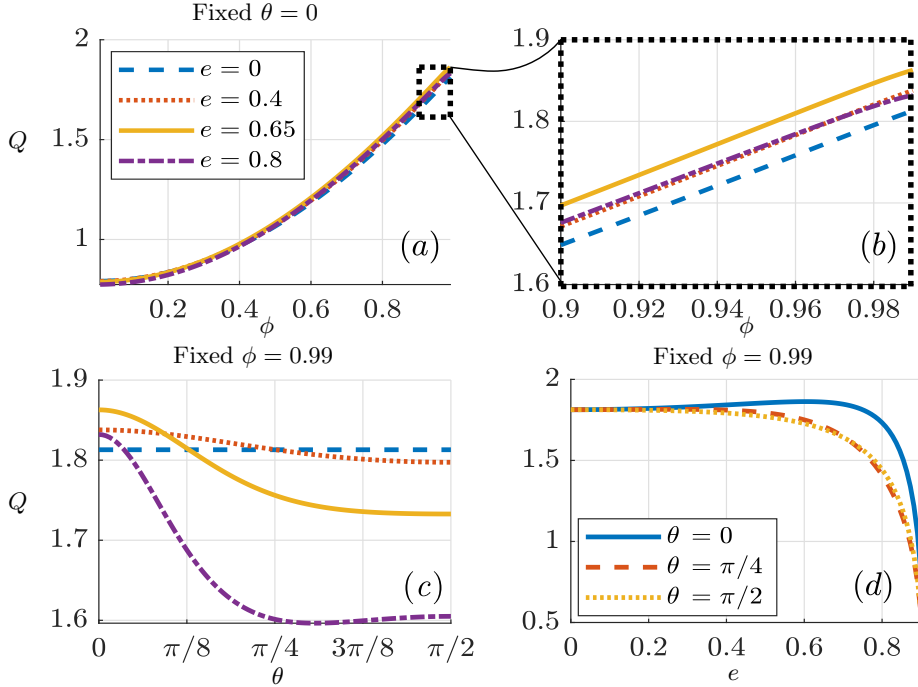


Figure 15: Dimensionless flow rate, Q , as a function of (a) and (b) offset, ϕ , (c) eccentricity, e , and (d), angular position, θ . Figure (b) displays the outlined section of (a). Here $R_o = 2$.

Q decreases monotonically with e . The results in Figure 15 suggest that $\phi = 0.99$, $\theta = 0$, and a non-zero value of e lead to the maximum flux.

Appendix D. Additional results (Section 4.2)

Figure 16a plots A_{zz} as a function of absolute offset, $1.45 \leq X \leq 1.8$, for $e_i = 0.7$, continuing the plot on Figure 9a for larger values of X . We observe the same line crossing behaviour noted for $e_i = 0.9$ in Figure 9a.

Figure 16b plots K_{xx} (dotted), K_{yy} (dashed), and K_{\min} (solid) for ellipses of eccentricities $e_i = 0$, $e_i = 0.7$, and $e_i = 0.9$, all oriented at angle $\Theta = \pi/2$. We see that over this range of offset values ($0 \leq X \leq 1.45$), $K_{\min} = K_{yy}$, and $\mathbf{k}_{\min} = \mathbf{e}_y$.

Figures 16c-h show either coupling or lift coefficients for $e_i = 0.7$ (left column) and $e_i = 0.9$ (right column) as functions of absolute offset, X . The dashed black lines are different Θ values, ranging from $\Theta = 0$ to $\Theta = \pi/2$ in steps of $\pi/40$. In each plot, the Θ value that maximises the force coefficient (over the majority of the X range) is indicated by a solid red line. Schematics indicate orientation for the minimal and maximal lines.

The coupling between rotation and translation in the x -direction is shown in Figures 16c-d. We see that for $\Theta = 0$ and $\Theta = \pi/2$, $C_x = 0$. Over the majority of the offset values, C_x is maximal when $\Theta = \pi/4$. However, for $e_i = 0.9$, there is a region close to the outer boundary, where smaller offset angles provide a higher coupling force.

The coupling between rotation and translation in the y -direction is shown in Figure

16e and Figure 16f. For both $e_i = 0.7$ and $e_i = 0.9$, C_y increases monotonically with Θ from $\Theta = 0$ to $\Theta = \pi/2$ over the full range of offset values.

The lift force, K_{xy} is plotted in Figure 16g and Figure 16h. This is zero for $\Theta = 0$ and $\Theta = \pi/2$ and maximal (over the majority of the offset values) for $\Theta = \pi/4$. However, for $e_i = 0.9$, as with C_x , there is a region close to the boundary, where crossing of the lines occurs.

With C_x for $e_i = 0.9$, near the wall it is a competition between coupling due to orientation and interaction with boundary. Distance and how much of ellipse is proximal.

Appendix E. Curvature matching (Section 6)

The equations for Γ_i and Γ_o are

$$\frac{((x - X) \cos \Theta + (y - Y) \sin \Theta)^2}{a_i^2} + \frac{((x - X) \sin \Theta + (y - Y) \cos \Theta)^2}{b_i^2} = 1, \quad (\text{E } 1a)$$

$$\frac{x^2}{a_o^2} + \frac{y^2}{b_o^2} = 1, \quad (\text{E } 1b)$$

respectively, where $a_{i,o}$ and $b_{i,o}$ can be calculated from $R_{i,o}$, $e_{i,o}$ via equations (3.2). We seek values for X , Y , Θ , and e_i so that the inner ellipse will touch the outer ellipse tangentially with matching curvature at a point

$$(x, y) = (a_o \cos \theta, b_o \sin \theta), \quad (\text{E } 2)$$

with its centre located furthest from the centre of the outer ellipse. Transforming coordinates

$$(x, y) \rightarrow \left(\frac{x}{a_o} \cos \alpha + \frac{y}{b_o} \sin \alpha, \frac{x}{a_o} \sin \alpha - \frac{y}{b_o} \cos \alpha \right) := (\tilde{x}, \tilde{y}), \quad (\text{E } 3)$$

where $\alpha = \pi/2 - \theta$. the equations for the inner and outer ellipse are then

$$\frac{(\tilde{x} \cos \tilde{\Theta} + (\tilde{y} - \tilde{Y}) \sin \tilde{\Theta})^2}{\tilde{a}_i^2} + \frac{(\tilde{x} \sin \tilde{\Theta} + (\tilde{y} - \tilde{Y}) \cos \tilde{\Theta})^2}{\tilde{b}_i^2} = 1, \quad (\text{E } 4a)$$

$$\frac{\tilde{x}^2}{\tilde{a}_o^2} + \frac{\tilde{y}^2}{\tilde{b}_o^2} = 1, \quad (\text{E } 4b)$$

We seek a geometry for the inner ellipse that touches the outer boundary in a single point, $(0, \tilde{Y})$ with matching tangent and curvature. As R is fixed, the major and minor axes of the ellipses are determined by their eccentricity values. To maximise the distance between the centres of the ellipse we take $\Theta = 0$ and the ellipse centres are a distance $1 - \tilde{b}_i$ apart. Therefore, we determine

$$\tilde{a}_i = R^{-2/3}, \quad \tilde{b}_i = R^{-4/3}, \quad \tilde{X} = 0, \quad \tilde{Y} = 1 - R^{-4/3}. \quad (\text{E } 5)$$

We can therefore determine the position and orientation angle of the initial ellipse by reversing the transformation (E 3). Some velocity colourmaps are shown in Figure 17. The values for θ and e_o in Figures 17a-h correspond to those in Figures 6e-l, respectively. This comparison shows that Q is larger for e_i, Θ that match the curvature of the outer ellipse (Figure 17), compared to $e_i = e_o$ and $\Theta = 0$ (Figure 6).

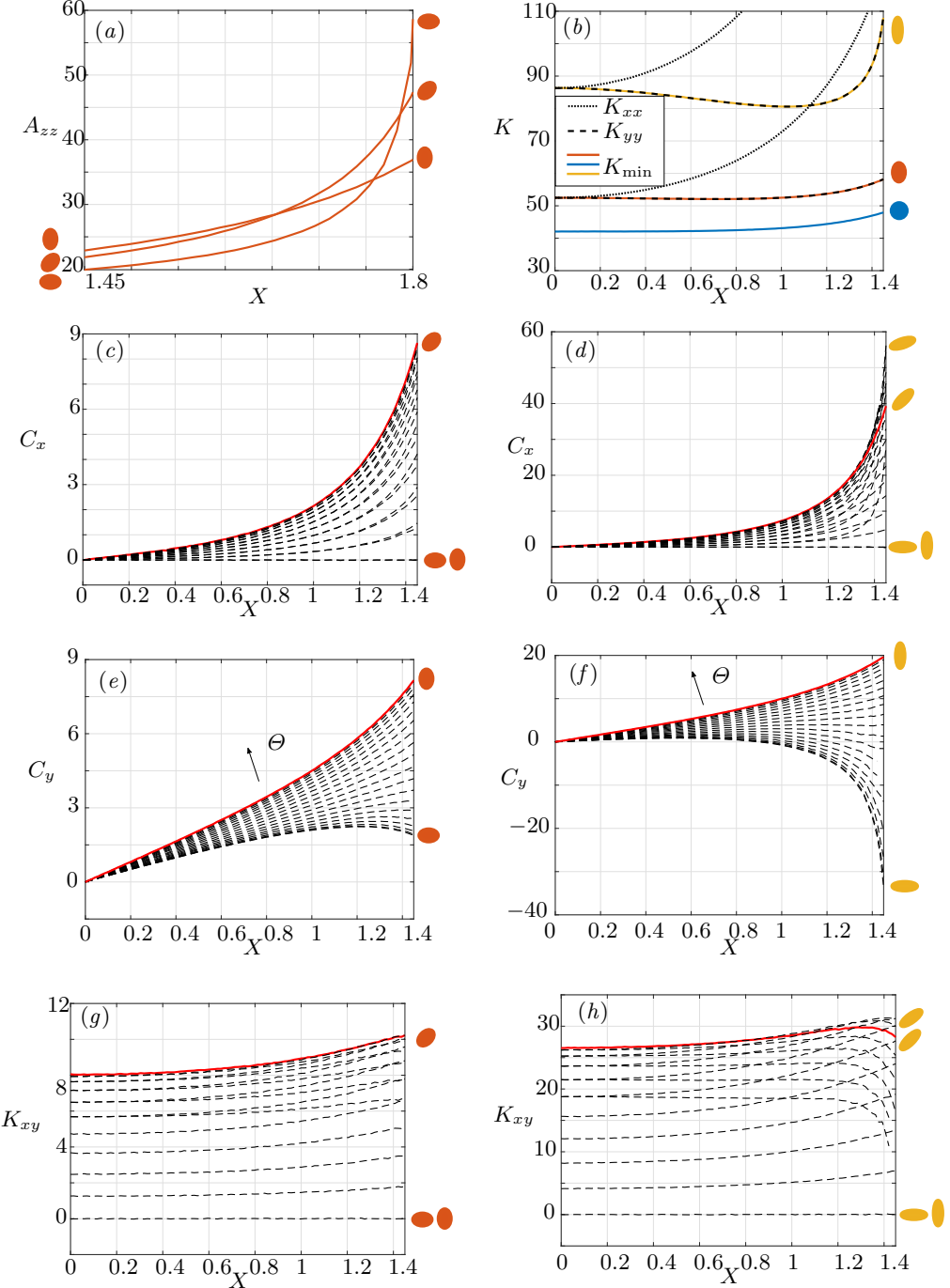


Figure 16: Figure (a) shows A_{zz} as a function of offset for $e_i = 0.7$ oriented at $\Theta = 0$, $\Theta = \pi/4$, and $\Theta = \pi/2$. Offset, $X \in [1.45, 1.8]$ (a continuation from Figure 9a). Figure (b) shows K_{\min} for $e_i = 0$, $e_i = 0.7$, and $e_i = 0.9$ all oriented at $\Theta = \pi/2$. Figures (c)-(h) show coupling and lift force coefficients for $e_i = 0.7$ (left column) and $e_i = 0.9$ (right column). Orientation angles vary between $\Theta = 0$ and $\Theta = \pi/2$ in steps of $\pi/40$.

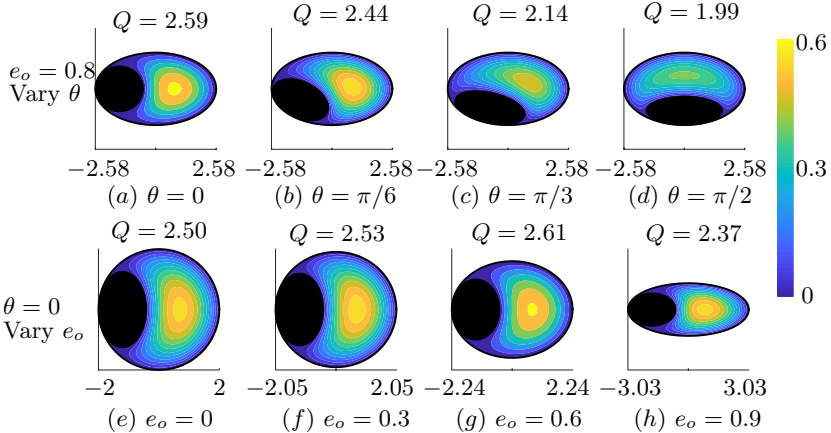


Figure 17: Dimensionless velocity colourmaps with dimensionless flow rates, Q . Axes are in (x, y) coordinates and these vary with eccentricity as the available space for fluid flow is constant. Plots (a)-(d) show the effect of the position of the inner ellipse, θ , and plots (e)-(h) show the effect of the outer ellipse eccentricity, e_o . Given θ and e_o , we solve for X_0 , Y_0 , and Θ_0 , so that the ellipses touch at a single point with matching tangent and curvature.

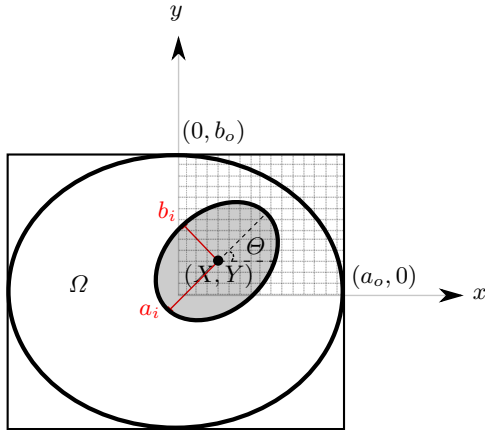


Figure 18: The outer ellipse has fixed eccentricity, $e_o = 0.6$, and characteristic radius, $R_o = 2$. The major and minor axes are $a_o \approx 2.2$ and $b_o \approx 1.8$, respectively. The inner ellipse has eccentricity $e_i \in [0, 0.9]$, and is centred at (X, Y) , where $X \in [0, 2.2]$ and $Y \in [0, 1.8]$. The inner ellipse is oriented so that its major axis makes an angle of $\Theta \in [0, 2\pi]$ with the x -axis.

Appendix F. Parameter sweep (Section 6)

Before solving the axial flow optimisation problem (outlined in Section 6 with more details in Appendix G) we considered whether a ‘curve hugging’ configurations would provide maximum flow for fixed e_o . We set $e_o = 0.6$ (and $R_o = 2$), and swept through the remaining four geometric parameters, e_i , X , Y , and Θ . For each configuration, we solved equation (2.35) subject to conditions (2.36) in `oomph-lib` (Heil & Hazel 2006). Due to the symmetry of the domain, it is necessary to only vary the position of the rod in a single (x, y) quadrant. Without loss of generality, we choose (X, Y) in Quadrant I (see Figure 18). We vary $e_i \in [0, 0.9]$, $X \in [0, a_o]$, $Y \in [0, b_o]$, and $\Theta \in [0, 2\pi]$. Not all these

configurations will be feasible, i.e. the ellipses will often intersect, so we select candidate geometries as those where the equation of the outer ellipse is negative on a fixed number of uniformly-spaced boundary points (we take $N = 1000$) of the inner ellipse.

F.1. Initial sweep

We initially swept through e_i , X , Y , and Θ with the following increments:

- $e_i = [0 : 0.1 : 0.9]$,
- $X = [0 : 0.1 : 2.2]$,
- $Y = [0 : 0.1 : 1.8]$,
- $\Theta = [0 : 2\pi/100 : 2\pi]$.

We calculate the maximum Q for each e_i , and plot this as a function of e_i in Figure 19a. The geometries and corresponding flow profiles are shown as inset diagrams for $e_i = 0$, $e_i = 0.5$, $e_i = 0.8$, and $e_i = 0.9$. This sweep allows us to identify ranges of X , Y , and Θ where the maximum Q occurs. We subsequently narrow our search to this region and reduce the step-sizes in X , Y , and e_i .

F.2. Finer sweep

Following the initial sweep, we narrow our search area to encompass only the region where maximum flow was achieved, and halve the step-sizes in X , Y , and e_i . We consider the following increments:

- $e_i = [0 : 0.05 : 0.9]$,
- $X = [0.9 : 0.05 : 1.4]$,
- $Y = [0 : 0.05 : 1.4]$,
- $\Theta = [2\pi(47/100) : 2\pi/100 : 2\pi(76/100)]$.

F.3. Results

In the results of both the initial and finer parameter sweeps, we see that maximum flow is achieved for $e_i = 0.8$ (Figures 19a and 19b). However, in the initial sweep, the steps in X and Y were too coarse to identify the true optimum geometry, and the geometry that maximised flux in Figure 19a was asymmetric. Refinement in the finer sweep allowed us to identify the symmetric optimum (Figure 19b) which is symmetric and touches the boundary tangentially in two locations, rather than a single point. Thus, we are motivated to explore the full optimisation problem, as the flux can be improved for a geometry that doesn't match curvature.

The lowest flux for a given e_i , $\min(Q)$, occurs when $(X, Y) = (0, 0)$ and $\Theta \approx 0$. A plot of $\min(Q)$ vs. e_i is shown with geometries and flow profiles indicated for $e_i = 0$, $e_i = 0.5$, and $e_i = 0.9$.

Appendix G. Optimisation constraints (Section 6)

From equations (6.3), we have that the equations of the outer and inner ellipses can be written respectively as

$$\mathbf{x}^T \mathbf{A} \mathbf{x} = 0, \quad \mathbf{x}^T \mathbf{B} \mathbf{x} = 0,$$

where $\mathbf{x} = (x, y, 1)^T$ and \mathbf{A} and \mathbf{B} are symmetric matrices of coefficients, functions of the components of \mathbf{g} (equation (6.1)). The intersections of two conics can be determined by considering their pencil, $\lambda \mathbf{A} + \mathbf{B}$ (Casey 1893). Conditions to determine the relative position of two ellipses were derived by Etayo & Gonzalez-Vega (2006), which we can

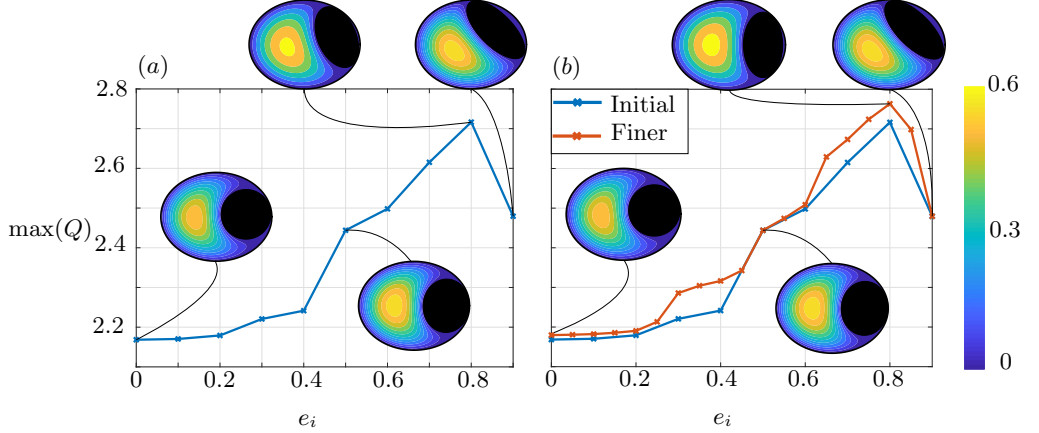


Figure 19: Plot of the maximum flux for each e_i value as a function of e_i . The inset flow profiles for $e_i = 0$, $e_i = 0.5$, $e_i = 0.8$, and $e_i = 0.9$ show the corresponding geometries and velocity profiles. The blue line shows results from the initial sweep, and the red line shows the results from the finer sweep.

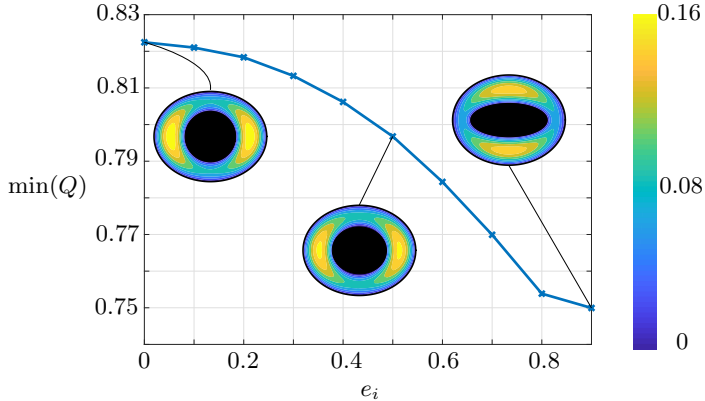


Figure 20: Plot of the minimum flux for each e_i value as a function of e_i . The inset flow profiles for $e_i = 0$, $e_i = 0.5$, and $e_i = 0.9$ show the corresponding geometries and velocity profiles.

then write in terms of the components of \mathbf{g} . The characteristic polynomial of the pencil (once turned monic) is

$$f(\lambda) = \lambda^3 + a\lambda^2 + b\lambda + c. \quad (\text{G } 1)$$

In order for the inner ellipse to be fully enclosed in the outer ellipse the following conditions must hold

$$a > 0, \quad -3b + a^2 > 0, \quad 3ac + ba^2 - 4b^2 > 0, \quad (\text{G } 2a,b,c)$$

$$-27c^2 + 18cab + a^2b^2 - 4a^3c - 4b^3 > 0, \quad (\text{G } 2d)$$

along with conditions

$$n_{22}\det(N) > 0, \quad \det(N_{11}) > 0, \quad (\text{G } 3a,b)$$

where $N = v\mathcal{A} + \mathcal{B} = (n_{ij})$ and N_{11} is the minor of N (Etayo & Gonzalez-Vega 2006). Equations (G 2) and (G 3) provide a set of six nonlinear constraints on \mathbf{g} . Thus, the optimisation problem can be formulated as

$$\min_{\mathbf{g}} \mathcal{R}, \quad \text{s.t. } \mathbf{c} > 0, \quad (\text{G 4})$$

where

$$\mathbf{c} = \begin{bmatrix} a \\ -3b + a^2 \\ 3ac + ba^2 - 4b^2 \\ -27c^2 + 18cab + a^2b^2 - 4a^3c - 4b^3 \\ n_{22}\det(N) \\ \det(N_{11}) \end{bmatrix}. \quad (\text{G 5})$$